Multi-Epoch 3D-Mapping-Aided Positioning using Bayesian Filtering Techniques

Qiming Zhong, Paul D Groves
University College London, United Kingdom

BIOGRAPHY

Qiming Zhong is a PhD student at University College London (UCL), specializing in 3D-mapping-aided GNSS. He holds a BSc in Electrical and Electronic Engineering from the University of Nottingham, Ningbo, China and an MSc in Robotics and Computing from UCL. (q.zhong.17@ucl.ac.uk)

Dr Paul Groves is an Associate Professor at UCL, where he leads a program of research into robust positioning and navigation. He is interested in all aspects of navigation and positioning, including multi-sensor integrated navigation, improving GNSS performance under challenging reception conditions, and novel positioning techniques. He is author of the book Principles of GNSS, Inertial and Multi-Sensor Integrated Navigation Systems. He is the recipient of the 2016 Institute of Navigation Thurlow Award and a Fellow of the Royal Institute of Navigation. He holds a bachelor's degree and doctorate in physics from the University of Oxford. (p.groves@ucl.ac.uk)

ABSTRACT

In dense urban areas, conventional GNSS does not perform satisfactorily, sometimes resulting in errors of tens of metres. This is due to the blocking, reflection and diffraction of GNSS satellite signals by obstructions such as buildings and moving vehicles. The 3D mapping data of buildings can be used to predict which GNSS signals are line-of-sight (LOS) and which are non-line-of-sight (NLOS). These data have been shown to greatly improve GNSS performance in urban environments. Location-based services typically use single-epoch positioning, while all pedestrian and vehicle navigation applications use filtered solutions. Filtering can reduce the impact of noise-like errors on the position solution. Kalman filtering-based solutions have been adopted as one of the standard algorithms for GNSS navigation in many different products, and particle filtering has been demonstrated by several research groups. This paper mainly investigates the performance of different filtering algorithms combined with 3D-mapping-aided (3DMA) techniques. In addition to the Kalman filter and particle filter, the grid filter is also considered. In contrast to a particle filter, the hypotheses of a grid filter are uniformly distributed (forming a grid), but with different likelihoods, which better fits the physics of the problem. At the same time, this allows the current UCL's single-epoch 3DMA GNSS positioning algorithm to be easily extended to multi-epoch situations. This paper then compares the performance of these continuous positioning algorithms in urban environments.

The datasets used for testing include pedestrian and vehicle navigation data, covering two main application scenarios that often appear in cities. Pedestrian navigation data is static, and was collected in the City of London using a u-blox EVK M8T GNSS receiver. The vehicle navigation data consists of GPS and Galileo measurements, collected in Canary Wharf by a trials van with a Racelogic Labsat 3 GNSS front end. Subsequently, these data are fed into several single- and multi-epoch filtering algorithms, including single-epoch conventional GNSS, single-epoch 3DMA GNSS, conventional extended Kalman Filter (EKF), conventional particle filter (PF), 3DMA GNSS particle filter (PF), and 3DMA GNSS grid filter (GF).

The results show that filtering has a greater impact on the results of mobile positioning with significant movement compared to static positioning. In vehicle tests, the conventional multi-epoch GNSS algorithms improve positioning accuracy by more than 40% compared to single-epoch GNSS, whereas in static positioning they deliver a limited improvement. 3DMA GNSS significantly improves positioning accuracy in the denser environments, but provides little benefit in more open areas. The 3DMA GNSS techniques and the filtering algorithms benefit each other. The former provides the latter with a better position solution at the measurement update step, while the latter in turn repays the former with a better initial position and a smaller search area. In vehicle tests at Canary Wharf, the 3DMA GNSS filtering reduces the overall solution error by approximately 50% and 40% compared to the single-epoch 3DMA GNSS and filtered conventional GNSS, respectively. Thus, multi-epoch 3DMA GNSS filtering should bring maximum benefit to mobile positioning in dense environments. The results from both datasets also confirm that the performance of 3DMA GNSS particle filtering and grid filtering are similar in terms of positional accuracy. In terms of efficiency, 3DMA GNSS grid filtering uses fewer particles to achieve the same coverage of the search area as particle filtering.

I. INTRODUCTION

Navigation and positioning are indispensable in modern life, and GNSS is one of the most widely used technologies. The demand for and potential of navigation and positioning services in urban canyons are enormous. Location-based services and applications have penetrated into many aspects of people's lives, such as travel, entertainment, and health [1]. In recent years, positioning modules have built into a wide range of consumer products such as smart watches and smartphones, making it easy for people to access their location. The involvement of location information has made many existing applications smarter and easier to use, while also giving rise to many new applications. Some sports apps on mobile phones, for example, record the trajectory of the runner and allow photos taken along the way to be attached. These services and applications, in turn, promote the demand of positioning methods for consumer-level equipment that achieves metres-level horizontal accuracy without additional computing resources and power consumption [2]. However, the performance of GNSS in cities is not satisfactory. According to a survey of Android customers in 2018, the low performance of positioning in cities has become a primary concern for users [3].

There are several reasons for the poor performance of GNSS in cities. In an environment known as an urban canyon, traffic circulates in the streets, and many buildings stand on each side of the street. The complex environment makes the full capabilities of GNSS almost impossible to realise. Tall buildings, large vehicles, and leafy trees all affect satellite signals to varying degrees. These conspicuous obstacles may attenuate, block, reflect, and diffract satellite signals, which may cause weak signals, poor satellite geometry, multipath effects, and non-line-of-sight (NLOS) reception [4–6]. Therefore, the performance of conventional GNSS is greatly impaired in urban canyons [4,7]. In such cases, the error of its position solution may reach tens of metres, which will largely degrade the quality of some location-based services. Among these negative factors, multipath interference and NLOS reception occur frequently in cities [8], and have been considered to be the two key reasons that restrict the performance of conventional GNSS positioning [9–13].

The emergence of 3D mapping data provides additional information for navigation and positioning, and also enriches methods for dealing with issues such as multipath and NLOS reception that often occur in urban environments. Those 3D models are often used to predict, at any given location, which satellite signals are directly visible and which are blocked by obstacles, and even in some implementations, to estimate path delays. It certainly provides additional useful information for positioning. The methods for implementing 3DMA GNSS are flexible and varied. According to the different principles of solution determination, the positioning and navigation algorithms using 3D mapping data can be divided into shadow matching and 3DMA ranging. The former uses the signal strength measurements, while the latter uses pseudo-range measurements as with conventional GNSS positioning. In the past few years, many different 3D-mapping-aided (3DMA) GNSS techniques [10, 11, 14–19] have been demonstrated to significantly improve the performance of GNSS in cities.

Location-based services typically use single-epoch positioning, while all pedestrian and vehicle navigation applications use filtered solutions. Compared to single-epoch solutions, filtered solutions are less affected by noise-like errors that occur during the measurement process. Currently, filtering algorithms commonly used in positioning and navigation include the extended Kalman filter (EKF) and the particle filter (PF), both of which can handle the case of non-linear distribution of state estimates. The involvement of 3D mapping data may be able to further improve positioning performance. Based on the characteristics of UCL's 3DMA GNSS core algorithm [14], this paper demonstrates two GNSS filters embedded with the 3DMA algorithms for multi-epoch case, namely the 3DMA particle filter (PF) and the 3DMA grid filter (GF). The main difference between them is the method used to represent the state estimates. The former uses an unevenly distributed set of particles with equal likelihood (after the resampling step), while the latter uses a uniformly distributed set of particles with different likelihoods.

Two GNSS datasets are used to test the algorithms mentioned in this paper. The signals in the first dataset were collected with an EVK M8T GNSS receiver in the City of London, which represents a traditional European city with predominantly masonry buildings. The other dataset was recorded with a Racelogic Labsat 3 GNSS front end in the Canary Wharf area of London, which has many glass-covered tall buildings similar to those found in North American and Asian cities.

This paper starts with the problem of GNSS in urban positioning and briefly reviews the various 3DMA GNSS positioning techniques. Then, detailed descriptions of multi-epoch 3DMA GNSS algorithms based on particle filtering and grid filtering are given in Section III. Section IV shows the positioning results from, respectively, single-epoch conventional GNSS, single-epoch 3DMA GNSS, multi-epoch conventional filtering, and multi-epoch 3DMA filtering in the two test environments, followed by a comparison and analysis of the results of these algorithms. Finally, Section V presents conclusions and Section VI recommends topics for future work.

II. BACKGROUND

II.1. Urban Positioning Problems

The accuracy of the positioning solution is subject to the ranging error and the geometry of the visible satellites [8]. Under good reception conditions, such as an open environment without obstructions, the error of the conventional GNSS positioning solution is generally within 10 metres [8, 20]. However, the maze of streets and buildings in the dense city would have a

significant impact on the satellite geometry and the propagation of GNSS signals, which may cause the positioning error to soar to tens of metres. Blocking and reflection by the buildings are considered to be the main reasons for the deterioration in positioning accuracy [9, 21].

One of the direct impacts of blocking on GNSS positioning is the reduction in the number of LOS satellites available. Conventional single-epoch GNSS algorithms require at least four satellites to calculate a position solution, and more measurements to perform outlier detection algorithms [8, 12]. In multi-epoch positioning, the insufficient number of observed satellites leads to increased uncertainty in the solution, which may affect performance. Most modern receivers are able to simultaneously track satellites from multiple constellations to capture more LOS signals, which alleviates the shortage of available signals to some extent [21].

The unhealthy geometric distribution of observed satellites is also one of the problems posed by blocking that may affect GNSS performance. If the satellite geometry is not satisfactory, even if the receiver can capture many LOS satellites, the accuracy of the solution in some directions will still suffer a great decline [8]. In a typical urban canyon, many obstructions, such as dense and tall buildings on both sides of the road and large vehicles on the road, block signals from perpendicular to the street direction and leave only a small portion of the sky overhead unobstructed, resulting in the majority of LOS satellites being distributed along the street. This unhealthy distribution often leads to a sharp increase in errors perpendicular to the street [22].

In addition to blocking, reflection effects interfere with GNSS positioning. In cities, especially emerging ones, glass and metal are used more widely on the outer surface of buildings. Large sheets of glass are metallised to strengthen them and are powerful radio reflectors that can easily reflect GNSS satellite signals [21]. Users may receive a mixture of LOS satellite signals and corresponding reflected replicas from smooth buildings and the ground at the same time, which is called multipath interference [8, 12, 21, 23]. The difference in the distance travelled by the reflected and LOS signals results in unsynchronized peaks of the code correlation function. Therefore, after the direct and reflected signals are mixed, the resultant signal received by the receiver is distorted, and it may be difficult to distinguish the reflected part from it. As a result, the distorted signal causes a certain range error, which leads to impaired GNSS performance. In addition, the measurements of the carrier phase, Doppler shift, and signal strength may be impacted by multipath effects [9].

The phenomenon of non-line-of-sight (NLOS) reception is the simultaneous occurrence of reflection and blocking. In other words, the LOS signal is blocked, and the user can only receive the reflected replicas. Since reflection may significantly increase the signal propagation path, NLOS reception would introduce considerable positive errors of tens of metres, or even thousands of metres in some extreme cases [8, 21, 22]. The NLOS signal strength varies drastically. Some are weak, while others are as strong as ordinary LOS signals [9, 24].

Multipath interference and NLOS reception, which occur frequently in urban canyons [8], are two key reasons that restrict the performance of conventional GNSS positioning [9–13].

II.2. 3D Mapping

The additional information that 3D mapping data can provide for positioning and navigation, including but not limited to terrain height, building location, building orientation and roof height, enriches and enables new methods for dealing with issues such as multipath and NLOS reception that often occur in urban environments.

Some studies [24, 25] show that the terrain height is a helpful supplement to the geometric distribution of satellites to improve the accuracy of positioning. It can be integrated into the conventional least-squares method as a virtual measurement. In dense cities with poor satellite geometry, terrain height aiding significantly improves the horizontal and vertical accuracy of the position solution, while in a relatively open environment, it only contributes to the accuracy in the vertical direction. The prerequisite for the terrain height aiding to be effective is that the accuracy of the terrain height obtained from the digital terrain model (DTM) is higher than that of the pseudo-range measurement. The application scenarios of this scheme are somewhat limited. It is suitable for situations where the height of the receiver above the ground is known, such as land navigation.

In addition to terrain height data, 3D building models are often used to assist in positioning. These models can be used to not only predict the visibility of satellites at a given position, but also estimate the distance travelled by the signal. There are many algorithms for predicting satellite visibility. For example, some algorithms look for the intersection between the ray from the candidate location to the satellite and the surface of nearby buildings [26], and some generate virtual fisheye skyline images using satellite and aerial imagery at candidate locations [27]. However, when a large number of candidates need to be considered, these methods require a large amount of computing resources and are not suitable for real-time positioning. A method of pre-calculating the building boundary (i.e. the lowest elevation angle above which the satellite signal is direct LOS) on a series of candidate points is proposed in [22, 28]. When needed, satellite visibility can be quickly obtained by comparing the satellite elevation with the pre-computed building boundary. The candidate points are determined in advance and cannot be changed during positioning, which loses some flexibility. The estimation of the signal propagation path usually uses the theory of geometric optics, which is more computationally intensive than visibility prediction. Examples include [11, 29–32].

Since implementation requires a lot of computing power, they may be subject to hardware performance (e.g. high-performance processing unit) and/or make some compromises (e.g., only single or double reflections are considered). In the restricted situation where the buildings on each side of the road are distributed in a strictly symmetrical manner, a more efficient method using symmetry to calculate the path delay of the NLOS signal is proposed [33].

According to the different principles of solution determination, the positioning and navigation algorithms using 3D mapping data can be divided into shadow matching and 3DMA ranging. The former uses the signal strength measurements, while the latter uses the pseudo-ranges similar to the conventional GNSS method.

Shadow matching adopts the idea of pattern matching and determines the solution by comparing the received signal strength with the satellite visibility prediction at a series of candidate positions. The concept was independently proposed by four different research groups [4, 34–36], and the authors of [17, 37] then initially demonstrated the potential of shadow matching technique in cross-street positioning with an accuracy of several metres. All of the different research groups that have worked on shadow matching have converged on the approach of hypothesis testing. The main difference lies in the methods of scoring candidate positions and obtaining the overall position solution from the candidate position scores. In the early research [38, 39], the measured satellite visibility is a binary value obtained by a hard threshold on the SNR value. The degree of matching between the visibility prediction and measurement uses the exclusive not or (XNOR) logical operation that returns true if its inputs are the same, otherwise false. The position solution is determined by a weighted average of the coordinates of several candidate points with high scores. Some subsequent studies [17, 22, 40, 41] have shown better performance using probability-based satellite visibility and Bayesian theory-based matching determination. Some different research groups have also demonstrated continuous positioning based on particle filtering [40, 42, 43].

There are many different approaches to 3DMA ranging. Among them, one of the most intuitive approaches is to exclude the NLOS signals detected by using 3D models from the calculation [44–46]. These methods require a fairly accurate initial position to enable subsequent NLOS detection algorithms to confidently predict satellite visibility without much time. In urban environments, most positioning applications cannot provide a sufficiently accurate solution within a few seconds after launching. Therefore, these methods are mostly used in continuous positioning.

Many research groups tend to use NLOS measurements instead of simply deleting them. Hypothesis testing is one of the commonly used methods. At a series of candidate positions generated around a rough position solution, the path delay of the NLOS signal can be estimated by the 3D building model. These candidate positions are then scored based on the path prediction and the actual measurement [15, 29, 31, 32, 47]. However, the primary limitation of these approaches is that the propagation path calculation requires a large amount of computing resources. The pseudo-range error distribution of the LOS signal conforms to a symmetric distribution, while the counterpart of the NLOS signal is asymmetric. A version of likelihood-based ranging is proposed [48] to use a different combination of error distributions at each candidate position based on the visibility predictions from 3D mapping data, which enables those NLOS pseudo-ranges to participate in the position calculation without explicitly computing the additional distance travelled by the them.

II.3. UCL's 3DMA GNSS Core Algorithms

UCL's 3DMA GNSS algorithms consist mainly of shadow matching, likelihood-based ranging and an integration algorithm, as shown in Figure 1. Both shadow matching and likelihood-based ranging are performed in the way of hypothesis testing on the candidate positions. The candidate positions are a set of three-dimensional coordinates. For land positioning and navigation applications, in order to reduce the complexity of the problem, the height dimension is set to the sum of the terrain height at that horizontal position and the height of the user device above the ground.

3D mapping data is used to predict the visibility of each satellite signal (i.e., LOS or NLOS) at each candidate position. This step is relatively computationally intensive and time consuming. Therefore, an intermediate product called building boundaries has been introduced to achieve the goal of being able to operate in real time over a large number of candidate positions. The building boundary refers to the maximum elevation of all buildings within a certain distance at a given azimuth. In other words, it is the minimum elevation of a satellite that allows users to receive its signals directly in that direction. The building boundary is pre-computed and stored for each candidate position. When required, the signal can be classified as LOS or NLOS by simply comparing the satellite elevation with the building boundary at the corresponding azimuth.

The shadow matching algorithm [17] compares the satellite visibility predictions with the counterpart determined by the received signal strength to calculate the degree of matching at different candidate positions, thereby giving the optimal solution. The algorithm comprises the following steps [14, 17]:

- The predicted visibility of each satellite signal at each candidate position is obtained.
- For each received signal, the probability that it is direct LOS is determined from the measurement of the carrier-to-noise density power ratio, C/N_0, using an appropriate statistical model.

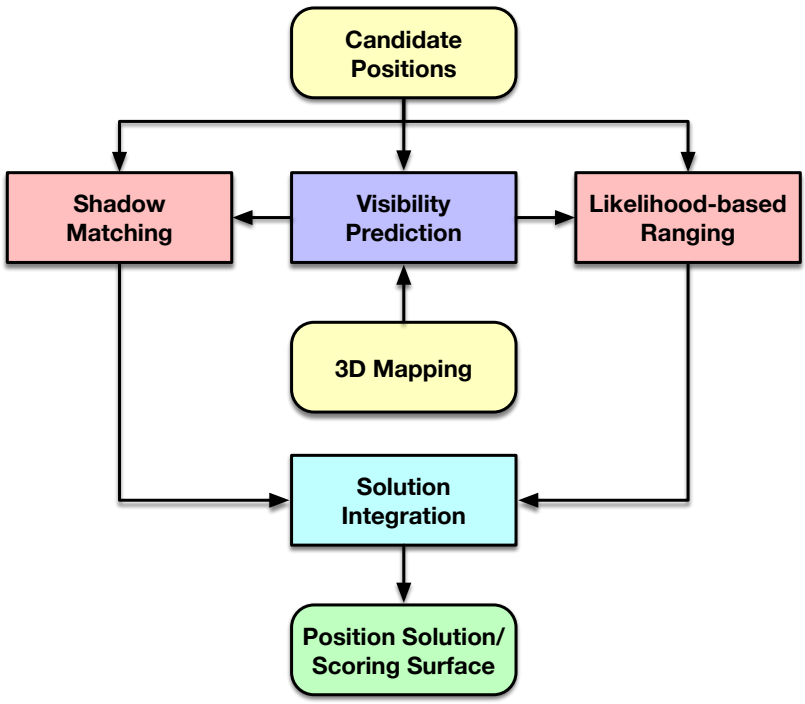

Figure 1: Components of the 3DMA GNSS Core Algorithms

- A matching score is obtained by evaluating each satellite at each candidate position based on the match between its predicted visibility and measured C/N_0.
- The final score for each candidate position is a combination of the matching scores for each satellite at that position.

The likelihood-based ranging algorithm [14] applies different statistical distributions to pseudo-range errors according to satellite visibility predictions, and then evaluates the correspondence between the measured and predicted pseudo-ranges to give the positioning solution. The algorithm comprises the following steps [14]:

- The predicted visibility of each satellite signal at each candidate position is obtained.
- At each candidate position, one of the satellites predicted to be direct LOS is selected as the reference.
- At each candidate position, the measurement innovation for each satellite is obtained by subtracting the direct LOS range and some known errors, such as satellite clock errors, atmospheric delays and inter-constellation offsets, from the measured pseudo-range, and then differencing with respect to the reference satellite to remove receiver clock offset.
- At each candidate position, the cumulative probability of the measurement innovation on a skew-normal distribution is determined for each satellite predicted to be NLOS. These NLOS innovations are then replaced by corresponding direct LOS innovations with the same cumulative probability.
- The final score for each candidate position is calculated using the modified measurement innovations and their error covariance matrix.

The intention of shadow matching is to improve the accuracy in the direction perpendicular to the street, whereas likelihood-based ranging is considered to be more accurate in the direction along the street. Therefore, a hypothesis-domain integration algorithm is executed to give a comprehensive single score for each candidate position based on the scoring surfaces from shadow matching and likelihood-based ranging. Finally, the position solution is obtained by using the combined scores to weight the candidate positions. Full details are given in Appendix A.1.

Single-epoch positioning using the 3DMA GNSS core algorithms described above has been demonstrated in the high-density central area of Canary Wharf [14].

II.4. Conventional Multi-epoch GNSS

All road and pedestrian navigation applications use filtered solutions. Filtering algorithms use the new measurements to correct the navigation solution predicted from previous information. Specifically, the previous clock drift and drift rate are used to predict the current counterparts, and the previous position and velocity solutions are used to give predictions of current position and velocity. Finally, the current measurements are used to correct the predictions to obtain the final solution.

The filtered solution mainly has the following three advantages. First, the code tracking noise can be smoothed, which also reduces the negative effects of multipath errors when moving. Second, since more information is available to compare each measurement with, the sensitivity of outlier detection can be improved. Finally, when the number of satellite signals is insufficient to determine the solution, or even all are shielded, the solution from the previous epoch can also maintain navigation with lower accuracy.

The extended Kalman filter and particle filter are the two most popular multi-epoch GNSS positioning techniques. The extended Kalman filter is a non-linear version of the Kalman filter, which linearizes the state transition and observation models using Taylor's theorem [8]. A particle filter is a sequential Monte Carlo estimation algorithm [8]. It uses a set of particles with equal likelihood to represent the estimated probability distribution of a set of states, regardless of the form of the distribution. Therefore, we expect filtering to also benefit 3D-mapping-aided GNSS over multiple epochs.

III. 3D-MAPPING-AIDED MULTI-EPOCH GNSS

As with conventional multi-epoch GNSS filters, the 3DMA GNSS filter needs to be able to handle non-linear state estimation. In addition, the 3DMA GNSS algorithm from UCL is built on a hypothesis testing approach that requires the filter to provide a range of position candidates. We therefore propose two different schemes, namely the 3DMA GNSS particle filter and the 3DMA GNSS grid filter. Compared to the extended Kalman filter, which assumes a Gaussian position distribution, the particle and grid filters offer better flexibility. In addition, they are more convenient for generating position candidates.

To represent the state estimates, the particle filter and the grid filter use different strategies, which is one of their most significant differences. Particles with equal likelihood are used by the particle filter, and the sparsity of their distribution determines the likelihood of a region. Conversely, the particles in the grid filter are distributed uniformly in a grid form, which directly describes the probability of their corresponding position being the solution. Figure 2 visualises the difference in the representation of position estimates between the particle filter and the grid filter, in which the colours of the particles represent their likelihood values and the blank areas represent buildings and locations outside the search area.

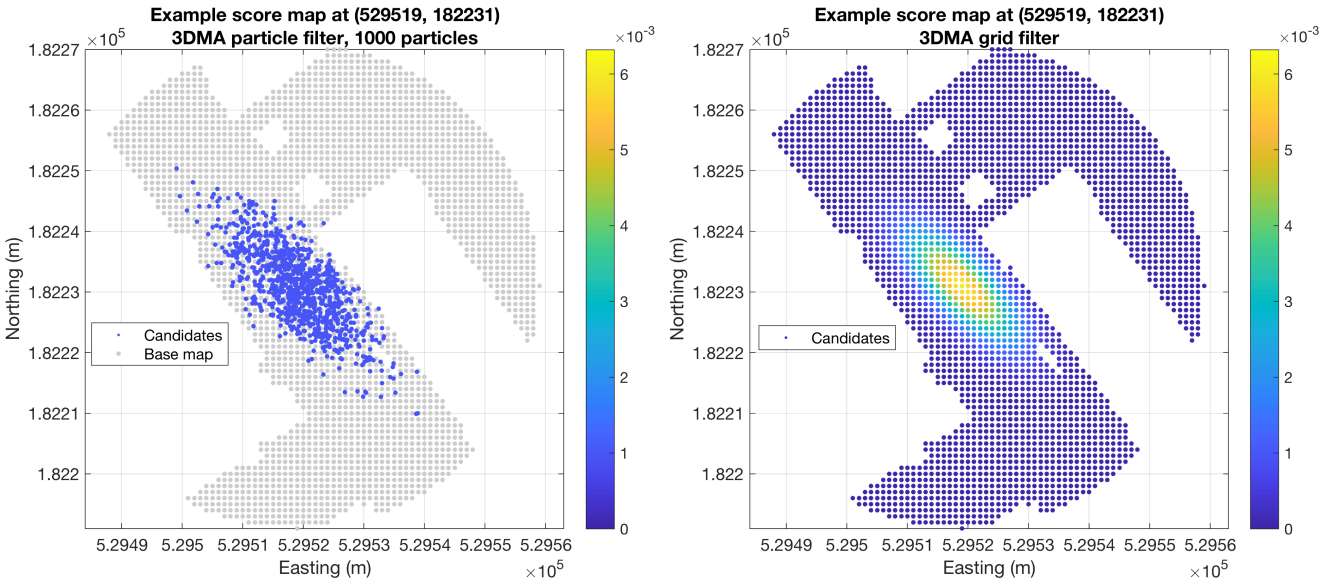

Figure 2: Different Representations of Position Estimates by Particle Filtering and Grid Filtering

III.1. 3DMA GNSS Particle Filter

As the name suggests, the 3DMA GNSS particle filter is an application of the conventional particle filter described in [8]. The conventional particle filtering scheme is naturally able to incorporate the 3DMA GNSS algorithms as its particles can play the role of position candidates. Figure 3 illustrates the six stages of the multi-epoch 3DMA particle filter implemented in this paper. Three of the components, i.e., system propagation, position measurement update and resampling, remain consistent with conventional GNSS particle filtering, while the initialisation, particle probability update and velocity filtering are modified to use 3D mapping data.

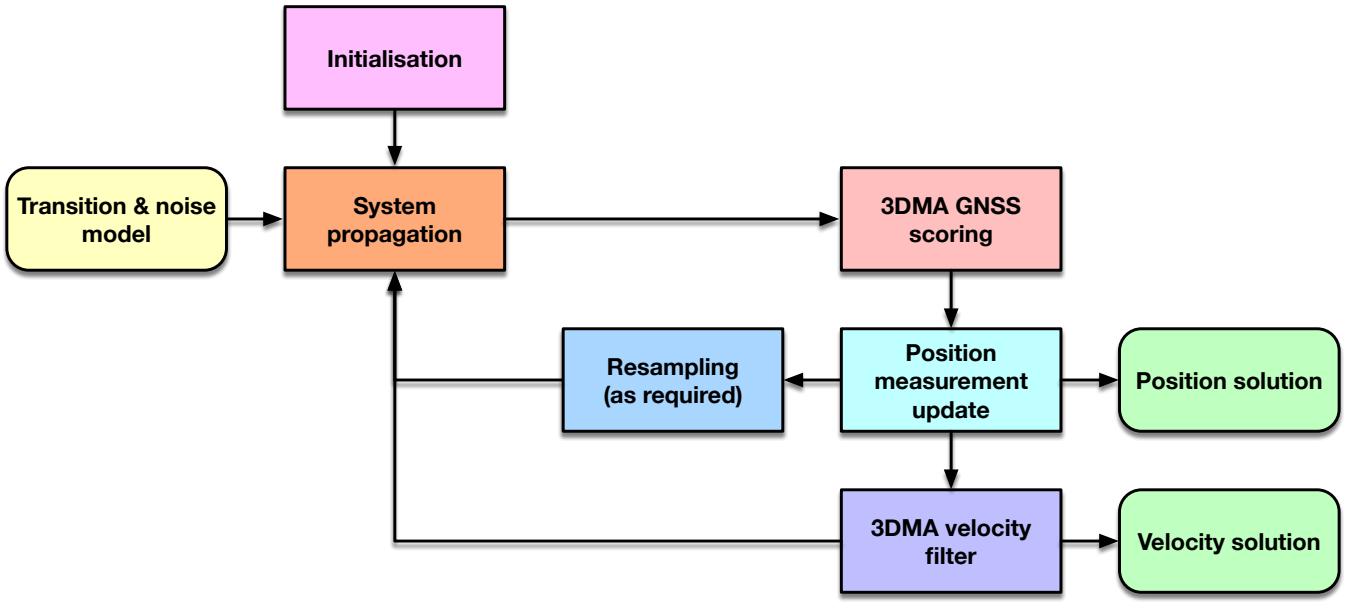

Figure 3: Components of a 3DMA GNSS Particle Filter

a. Initialisation

The initialisation is divided into two steps to initialise velocity and position respectively. For position initialisation, a standard single-epoch 3DMA GNSS algorithm set (as detailed in [14]) is used. The particle filter is capable of representing any shape of the probability distribution. Therefore, the position solution takes the form of a likelihood distribution rather than a position coordinate and its corresponding uncertainty. The position likelihood distribution is then sampled to generate a set of particles with equal probability. The number of particles, N, should be determined as appropriate, and the initial probability of each particle is assigned as $1/N$.

The velocity initialisation takes place after the initialisation of the position. The least squares algorithm is used to estimate the velocity and clock drift from the pseudo-range rate measurements. It weights the pseudo-range rate measurements based on the corresponding overall probability of being predicted to be direct LOS over all candidate positions. Pseudo-range rate measurements with LOS probabilities below a certain threshold are treated as outliers and removed. A relatively low threshold is applied to avoid situations where only a few or even no measurements with acceptable LOS probabilities are available to update the velocity in very dense cities. The velocity initialisation proceeds as follows:

- At each candidate position, satellite visibility is predicted.
- The direct LOS probability for each satellite is estimated based on the satellite visibility predictions for each particle and the corresponding 3DMA likelihoods.
- The satellite signals are selected and weighted according to their direct LOS probabilities.
- The velocity and clock offset solution is estimated by a least squares method.

Full details are given in Appendix A.2 a.

b. System Propagation

In the system propagation stage, the state estimate of each particle changes while its probability remains unchanged. The process is similar to conventional GNSS particle filtering. The particle state used here only contains the position (in easting and

northing form), while the velocity is considered separately in section III.1 e. First, the sampling of the system noise is performed independently for each particle. Each particle, $\mathbf{x}_{n,k}$, is then propagated separately through the system propagation model given by

$$\mathbf{x}_{p,k} = \phi_{k-1}(\mathbf{x}_{p,k-1}, \mathbf{w}_{p,k-1}) \tag{1}$$

where p denotes the p^{th} particle, k denotes the k^{th} epoch, ϕ_{k-1} is the transition function, and $\mathbf{w}_{p,k-1}$ is the randomly generated system noise vector based on the known probability density function (pdf) of $\mathbf{w}_{k-1}$. A simple system transition model that uses the velocity solution from the previous epoch to calculate the displacement is adopted in this paper. The displacement prediction is given by Equation (32) and its corresponding error covariance is given by Equation (33).

c. 3DMA GNSS Scoring

The next step is to apply the 3DMA GNSS core algorithms. The east-north coordinates of the particles are rounded to the nearest integer multiple of 1-metre grid spacing to reduce the computational load and then fed into the 3DMA GNSS algorithm as candidate positions. At each candidate position, the visibility of the observed satellites is determined from the 3D mapping data. Next, shadow matching and likelihood-based ranging algorithms are executed. The scores from these two algorithms are then combined by hypothesis-domain integration to give the 3DMA likelihood for each particle, $\tilde{\Lambda}_{p,k}$. Note that the particle here is equivalent to the candidate position in the 3DMA GNSS algorithm description. Full details are given in Appendix A.1.

d. Position Measurement Update

In contrast to system propagation, the measurement update phase changes the probabilities but not the state estimates. This step is processed in the same way as its counterpart in conventional GNSS particle filtering. However, the observation likelihoods, $\tilde{\Lambda}_{p,k}$, are different from those in a conventional measurement update. Thus, the likelihood calculated from 3DMA GNSS algorithms for each particle, $\tilde{\Lambda}_{n,k}$, is multiplied with its prior probability, $\Lambda^{-}_{n,k}$, to obtain a joint probability, given by

$$\Lambda'_{n,k} = \Lambda^{-}_{n,k}\tilde{\Lambda}_{n,k} \tag{2}$$

The updated probabilities of each particle are then obtained by renormalizing the likelihoods, giving

$$\Lambda^{+}_{n,k} = \frac{\Lambda'_{n,k}}{\sum_{n=1}^{N}\Lambda'_{n,k}} \tag{3}$$

The filtered position solution is then obtained by

$$\begin{aligned} \hat{E}^{+}_{k} &= \sum_{n=1}^{N}\Lambda^{+}_{n,k}E_{n,k} \\ \hat{N}^{+}_{k} &= \sum_{n=1}^{N}\Lambda^{+}_{n,k}N_{n,k} \end{aligned} \tag{4}$$

where $E_{n,k}$ and $N_{n,k}$ are the east and north coordinates of the n^{th} particle, respectively.

e. 3DMA GNSS Velocity Filter

Similar to the initialisation step, the position solution and the velocity solution are obtained separately. The velocity and clock drift are maintained by an extended Kalman filter. It is a two-step process. In the prediction step, the velocity state estimates between epochs remain unchanged as there is no information to propagate them, while their error covariance is increased to model the unknown acceleration between epochs and the unknown change in receiver clock drift. In the update step, the measurement errors are weighted based on the corresponding satellite LOS probabilities, with smaller standard deviation being given to measurement errors with higher LOS probabilities. In static positioning, the velocity filter can be omitted. Full details are given in Appendix A.2 e.

f. Resampling

The final phase of 3DMA particle filtering is resampling. As with conventional GNSS particle filters, the probability of many particles may shrink to zero after several consecutive recursions, leaving only a few particles with relatively large weights. Those low-probability particles crowd computational resources while reducing the number of particles used to represent the core features of the state estimate distribution, resulting in a decrease in estimate performance and efficiency. A particle filter is most efficient when its particles have a similar probability. Therefore, a resampling step is introduced to remove particles with

small weights and duplicate particles with significant weights to mitigate the particle degeneracy problem. Resampling can be performed every fixed number of epochs, or based on the degree of degeneracy, N_{eff}, given by

$$N_{eff} = \left[\sum_{n=1}^{N} \left(\Lambda_{n,k}^{+} \right)^2 \right]^{-1} \tag{5}$$

falling below a threshold. This paper adopts the latter option with a threshold of $4N/5$, below which resampling is performed. Finally, resampled particles are reallocated with equal probability, $1/N$.

III.2. 3DMA GNSS Grid Filter

Grid filtering uses a set of particles (also called samples) with different likelihoods, uniformly distributed over a certain search space, to represent the posterior distribution of some stochastic process given noisy and/or partial measurements. Focusing on the 3DMA grid filter used in this paper, the search space is a horizontal plane represented by the east-north position coordinates, and the likelihoods of the particles are determined by the 3DMA GNSS core algorithm. A multi-epoch 3DMA grid filter has six phases, shown in Figure 4. The Initialisation, 3DMA GNSS scoring and 3DMA velocity filter phases are equivalent to their 3DMA particle filter counterparts.

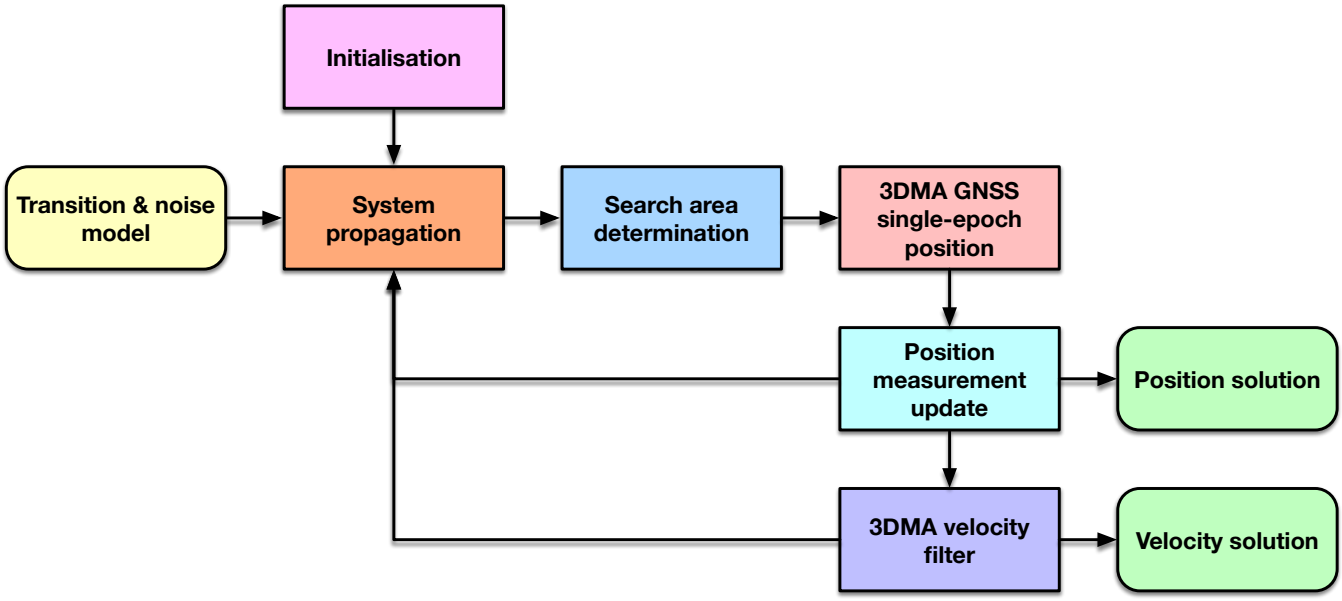

Figure 4: Components of a 3DMA GNSS Grid Filter

a. Initialisation

The Initialisation of the 3DMA grid filter is almost identical to the corresponding part in the 3DMA particle filter. A single-epoch 3DMA GNSS algorithm is executed to obtain a series of candidate positions and their likelihoods. The pseudo-range rate measurements are then weighted by the satellite LOS probabilities derived from the likelihoods and satellite visibilities at these candidate positions to initialise the overall velocity using the least squares method. Full details are given in Appendix A.2 a.

b. System Propagation

Position propagation is a process of predicting the state estimate of the next epoch based on currently known information, which moves position candidates and reassigns their likelihoods, which is conducted in three steps as follows:

- Search area extension.
- Motion-based likelihood redistribution.
- Confidence-based likelihood redistribution.

The candidates with high scores can be located anywhere in the search area. Updated position solutions for the current epoch

are more likely to appear in and around these high scoring regions than others. Therefore, the search area needs to be expanded large enough to allow high scoring candidates that fall far from the centre and their surrounding areas to be taken into account in the subsequent processing.

In the motion-based likelihood redistribution, the movement of the candidate positions is carried out according to the system transition model, reflecting the motion of the receiver. It is less likely that the position translation of the receivers exactly conforms to the grid. The translation between epochs is therefore split into an integer grid space and a remainder in the east and north directions respectively. For the integer part, the likelihood of each candidate position is inherited directly from its likelihood before the translation. For the remainder part, at each candidate position, the likelihood is collectively determined by the likelihoods within a certain range around it.

The confidence-based likelihood redistribution aims to add a small base likelihood for all candidates in the search area, as all candidates have the potential to be the final solution. The base likelihood in fact models the error of the 3DMA GNSS core algorithms, with larger values indicating less confidence in the solution given by the 3DMA GNSS algorithm. Full details are given in Appendix A.2 b.

c. Search Area Determination

After the system propagation step, the search area is expanded and the number of candidate positions grows to about four times its original size. The redefinition of the search area not only reduces the number of candidate positions but also centres the search area around the high scoring candidates. Full details are given in Appendix A.2 c.

d. 3DMA GNSS Scoring

The 3DMA GNSS scoring process is the same as the corresponding process of the 3DMA GNSS particle filter. The standard single-epoch likelihood-based 3DMA GNSS ranging, shadow matching and hypothesis-domain integration algorithms are used over the search area determined in the last step. The output will be a set of likelihoods for each candidate position in the search area, $\tilde{\Lambda}_{p,k}$, where p denotes the candidate position p, and k denotes the k^{th} epoch. Full details are given in Appendix A.1.

e. Position Measurement Update

The position measurement is updated in a similar way to the equivalent part of the 3DMA GNSS particle filter. The position likelihood distribution is updated to incorporate the new measurements from the current epoch, k. At each candidate position, the propagated likelihood, $\Lambda^{-}_{p,k}$, is multiplied by the likelihood, $\tilde{\Lambda}_{p,k}$, derived by the 3DMA GNSS algorithm based on the measurements of the current epoch k to obtain a composite likelihood. Either of the two likelihood surfaces with a higher confidence level will have a higher and narrower peak, making it more likely to dominate the composite distribution. In addition, a constant weighting parameter is introduced to adjust the dominance of the likelihood from the measurement in the combined distribution, regulating the receptivity of the filter to the new measurements. Finally, the position solution is obtained by using the combined scores to weight the candidate positions. Full details are given in Appendix A.2 d.

f. 3DMA GNSS Velocity Filter

The receiver velocities in the 3DMA grid filter are also maintained by a Kalman filter, which is implemented in the same way as in the 3DMA particle filter. Full details are available in Appendix A.2 e.

IV. EXPERIMENTAL TESTS

The first dataset consists of a number of 2-minute GNSS records from the three constellations of GPS, GLONASS and Galileo. They were collected at various locations in the City of London in July 2017 using a u-blox EVK M8T GNSS receiver at a recording frequency of 1 Hz. The antenna was maintained at a height of 1.1 metres above the ground. The experimental locations are marked in Figure 5. Note that at each test site, there are two sets of data collected in the morning and afternoon, which gives the satellites enough time to orbit to significantly different positions, allowing the morning and afternoon data to be independent of each other. Therefore, the afternoon dataset is used for tuning the configurable parameters of the positioning and filtering algorithms, while the morning one is used for testing. The City of London is a typical European city. The roads in such cities are generally narrow, and the walls of the buildings are mainly made of masonry.

The other dataset was collected in Canary Wharf in July 2019 by a van equipped with a Racelogic Labsat 3 GNSS front end. The measurement data was intermediate frequency samples and was subsequently processed by Focal Point Positioning. The dataset consists of 1602 epochs of GPS and Galileo measurements from conventional code tracking. Figure 6 illustrates the true trajectory of the trial vehicle provided by a Novatel iMAR INS/GNSS system. The vehicle departed from the lower right corner of the map, moved clockwise on the path in the direction indicated by the orange arrows, and traversed the northern area twice before finally returning to the vicinity of the starting point from the road on the right of the map. The central area of Canary Wharf is marked by a red rectangle in Figure 6. There are many high-rise buildings with glass and steel surfaces in this area,

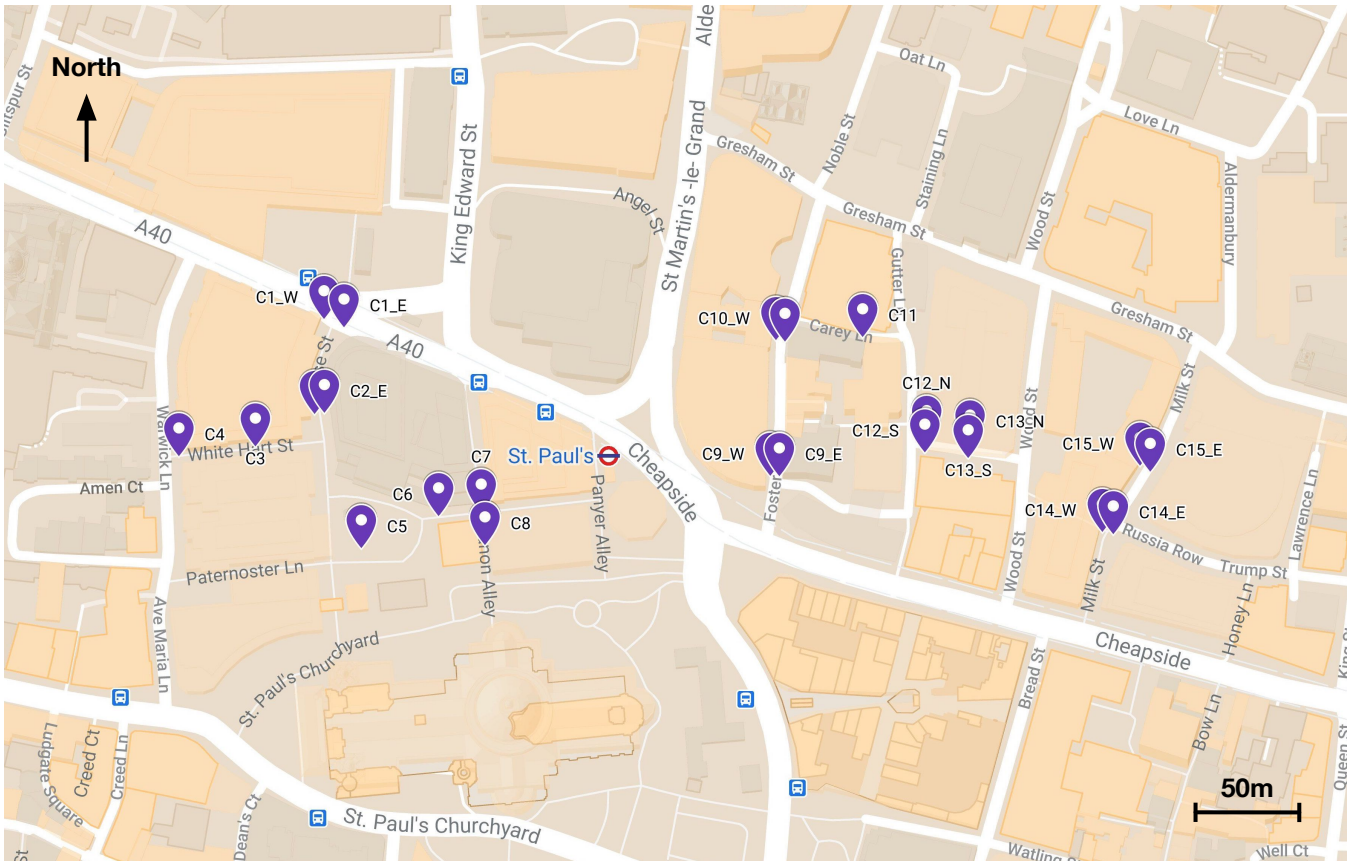

Figure 5: True positions in City of London. Background map ©Google Maps

which are common in some large cities in North America and Asia. The environmental characteristics in other areas of Canary Wharf are more open than those in the City of London.

In order to simulate navigation from different locations, the Canary Wharf dataset was divided equally into 8 segments of 200 1-second epochs each, marked with different coloured dots in Figure 6. Three of the eight segments occur throughout in the non-central areas, while the remaining five segments span both central and non-central areas, with two segments starting in the central area.

To evaluate the performance of multi-epoch 3DMA GNSS, the following six positioning algorithms were implemented, tested and compared in the two test datasets mentioned above:

- Single-epoch conventional GNSS with outlier detection and terrain height aiding
- Single-epoch 3DMA GNSS
- Conventional extended Kalman filter (EKF) with terrain height aiding
- Conventional particle filter (PF) with terrain height aiding
- 3DMA GNSS particle filter (PF)
- 3DMA GNSS grid filter (GF)

The single-epoch conventional GNSS algorithm is described in [14]. The single-epoch 3DMA GNSS algorithm is described in both [14] and Appendix A, and the parameters used can be found in Appendix A. The implementation of the conventional extended Kalman and particle filters can be found in [8]. The algorithms for 3DMA GNSS filtering are summarised in Section III and detailed in Appendix A.2. Note that the 3DMA GNSS core algorithm already includes an implicit terrain height aiding algorithm.

In general, it is better to separate the tuning and testing data. For the dataset collected in the City of London, the data collected

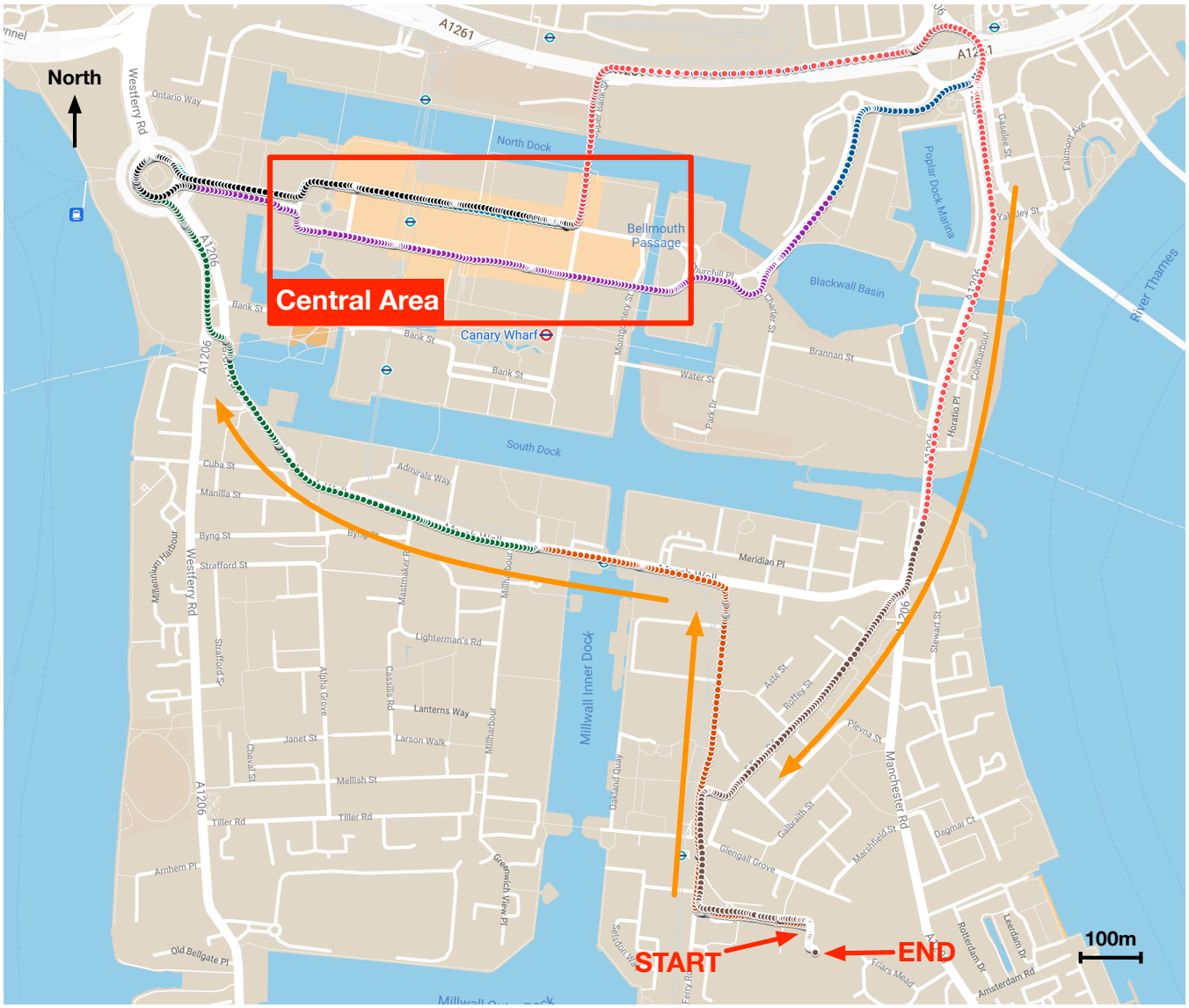

Figure 6: True trajectory of van trial in Canary Wharf, London. Background map ©Google Maps

in the afternoon was used to tune the parameters of the algorithms, while the morning data was used to test and generate the results presented in this section. However, for the Canary Wharf dataset, the same data was used to tune and test the algorithms due to the limited duration of the dataset.

Figures 7 and 9 show the root mean square (RMS) position errors obtained from tests on the City of London and Canary Wharf datasets respectively. As all methods include a terrain height aiding technique, only errors in the horizontal radial direction were assessed. Figures 8 and 10 illustrate the maximum positioning error at different confidence levels for the solutions of the City of London and Canary Wharf datasets respectively. The blue bars represent the maximum position error within the 90% confidence interval, i.e. the maximum error after excluding the 10% of solutions with the largest absolute errors. Similarly, the orange bars show the maximum error within the 50% confidence interval. It is worth noting that a very small number of faulty epochs were excluded from the single-epoch positioning in the vehicle test because the number of observed satellites did not meet the minimum requirements for running the least squares ranging algorithm. Detailed results are presented in Appendix B.

The results show that the conventional GNSS filtering algorithms perform better than the conventional single-epoch GNSS algorithm in most cases. In vehicle tests in particular, the overall root-mean-square (RMS) error in the position solution from even the worst performing multi-epoch GNSS algorithm, i.e., the conventional extended Kalman filter, is approximately 40% lower than that of the single-epoch conventional least squares. However, in the static positioning of the City of London dataset,

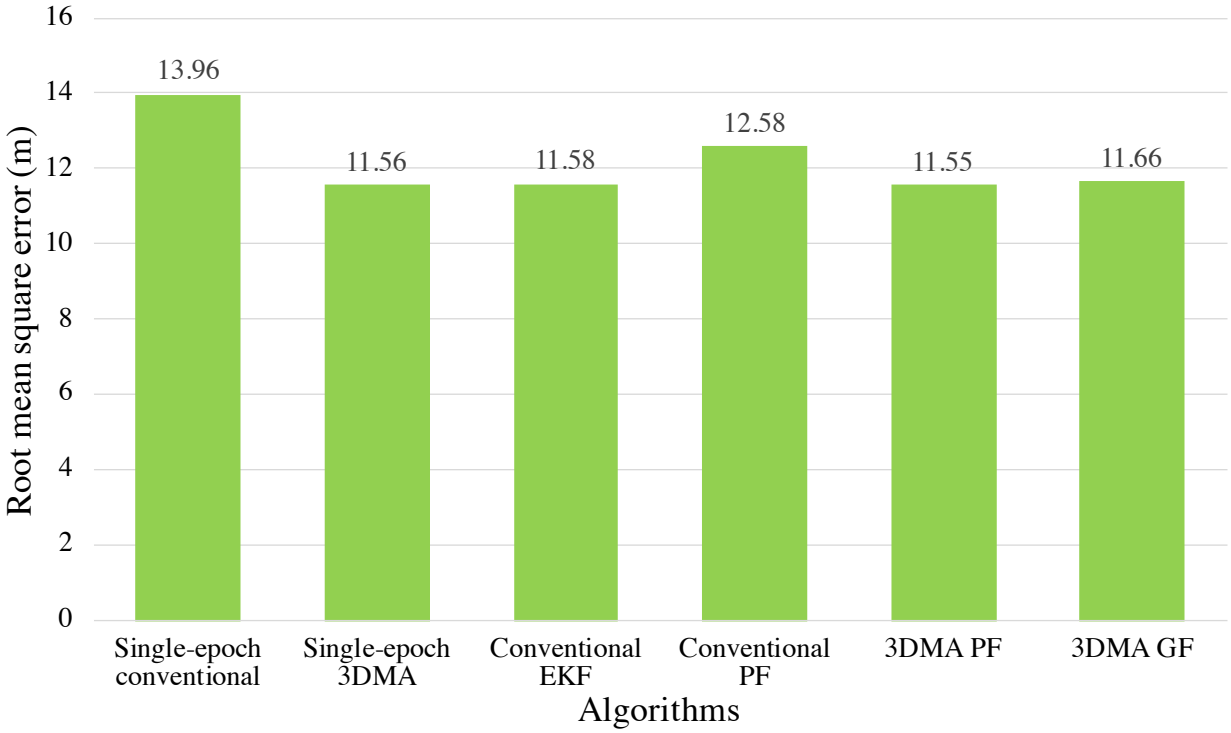

Figure 7: Horizontal radial position root mean square error in City of London (stationary)

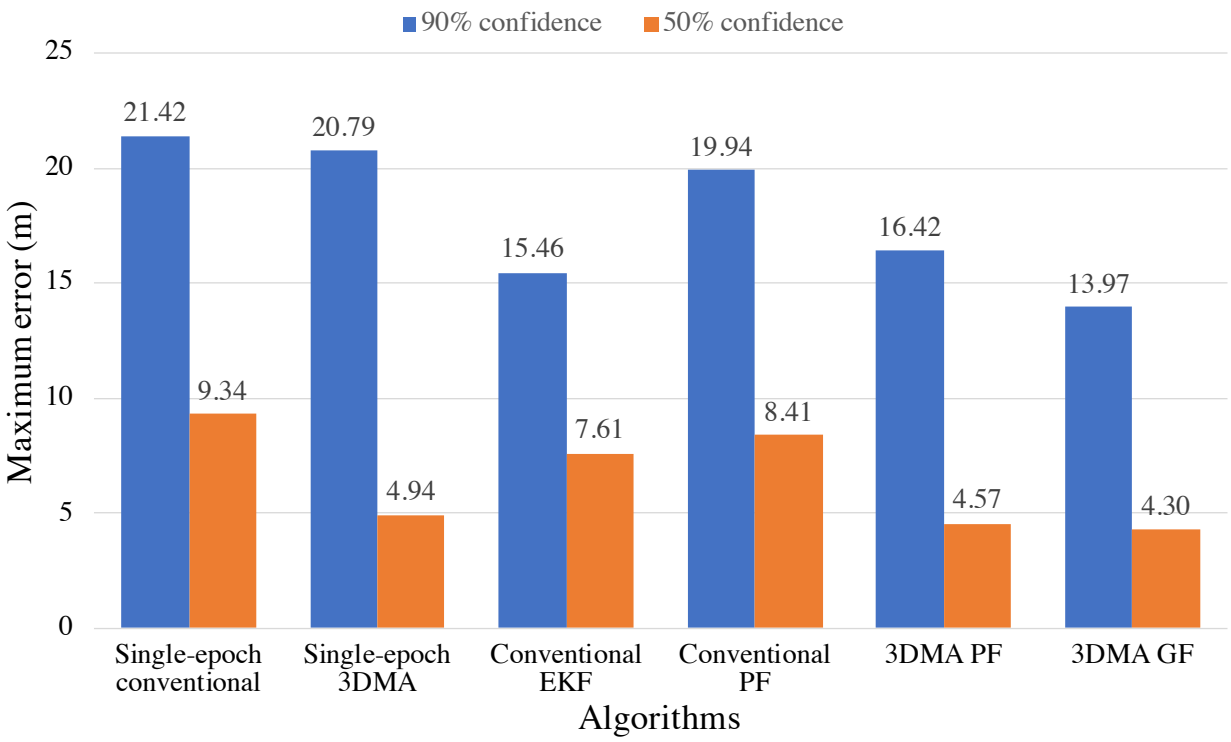

Figure 8: Maximum horizontal radial position error at various confidence levels in City of London (stationary)

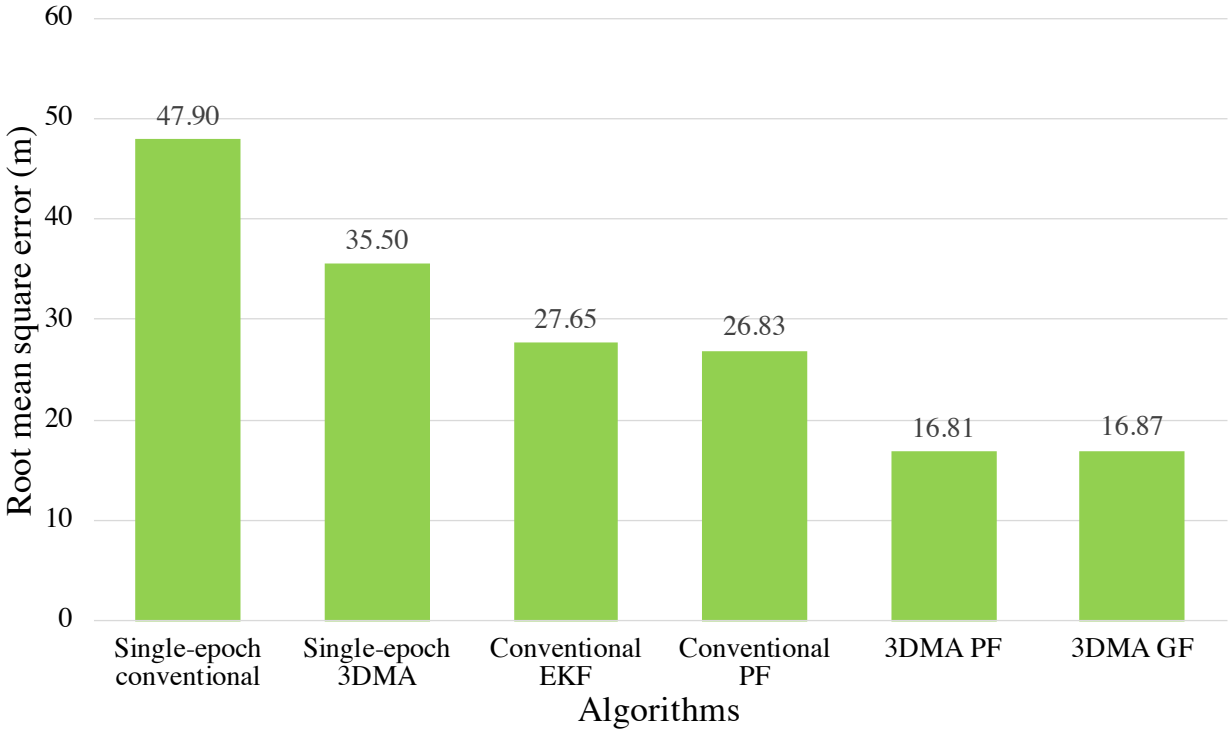

Figure 9: Horizontal radial position root mean square error in Canary Wharf (vehicle)

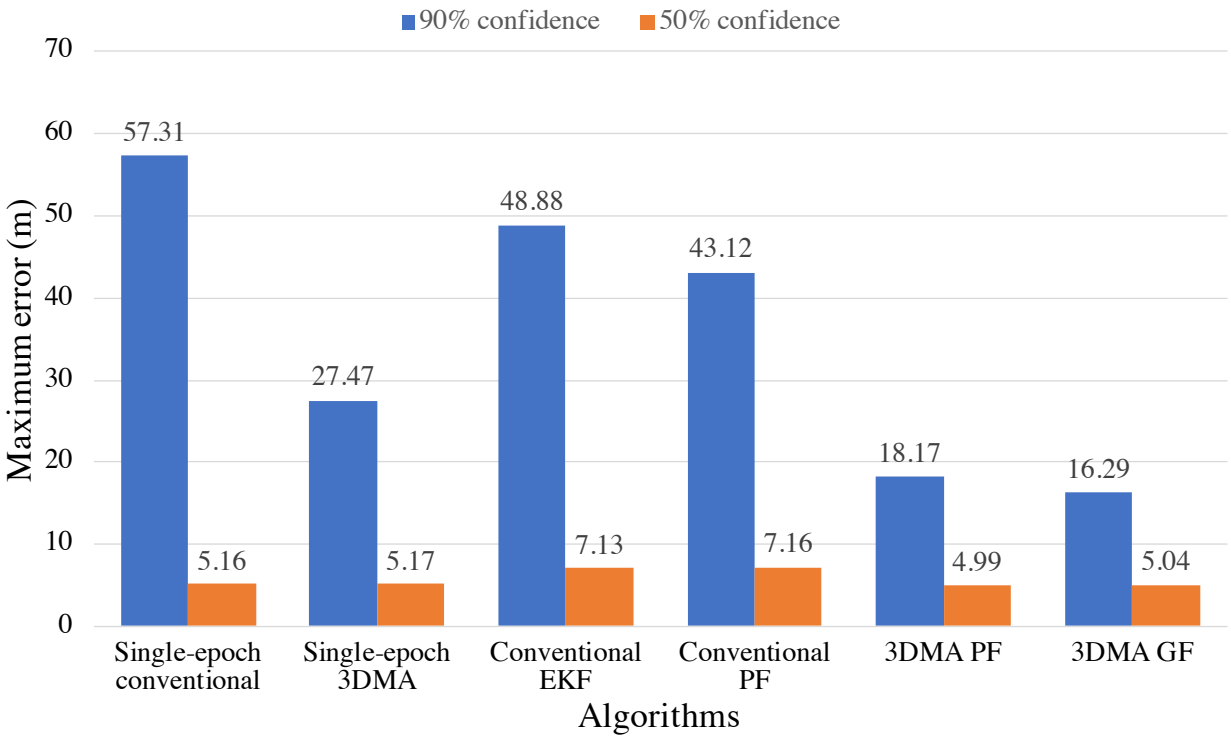

Figure 10: Maximum horizontal radial position error at various confidence levels in Canary Wharf (vehicle)

the RMS error of the filtered solution is just slightly reduced compared to the single-epoch GNSS, which is not as significant as in the vehicle tests. It is clear that filtering has a greater impact on the vehicle results. One possible reason for this is that for static positioning the NLOS and multipath errors are largely correlated over successive epochs, whereas for mobile positioning they vary more significantly and can thus be more easily mitigated by the filtering process.

With the use of the 3DMA GNSS techniques, the single epoch positioning algorithm improves significantly in vehicle tests. The overall RMS error of the single-epoch 3DMA GNSS position solution is reduced by about a quarter compared to the conventional one, while its maximum position error at 90% and 50% confidence levels is even lower than the conventional filtered results. It can be found from Table 6 in Appendix B that the single-epoch 3DMA GNSS performs better in segments with more epochs in the central region of Canary Wharf. This indicates that 3DMA GNSS is more advantageous in the denser environments than in the more open areas, which is also corroborated by the City of London results. In the City of London, the 3DMA GNSS techniques provide little improvement, with only an obvious reduction in error at the 50% confidence level compared to the conventional.

3DMA GNSS techniques and filtering algorithms benefit from each other. With the filtered solution providing a better initial position for the 3DMA GNSS algorithms in the Canary Wharf dataset, the position error of the filtered 3DMA GNSS solution is further reduced by about 53% compared to that of the single-epoch 3DMA GNSS. Compared to the results of the conventional filtering solutions, the filtered solutions with the 3DMA GNSS techniques show a reduction of approximately 40% and 60% in, respectively, the overall RMS error and the maximum error at 90% confidence. Particularly in the denser environments, such as epochs 1001-1200, 3DMA GNSS reduces the error in the filtered solution to approximately one third of the conventional filtered solution. In the City of London dataset, where 3DMA GNSS performed unsatisfactorily, the introduction of 3DMA GNSS provides little benefit to the filtering.

Comparing the results from the filtered 3DMA GNSS algorithms, it can be seen that the overall accuracy of the filtered solutions from grid filtering and particle filtering are similar to each other for both static positioning in the City of London and vehicle navigation in Canary Wharf. This is in line with expectations that grid filtering essentially uses the likelihood of a grid of candidate points to represent the distribution density of particles at these candidate positions, which would not change the performance in terms of positional accuracy. Figures 8 and 10 show that the maximum position error of the grid filter solution at the 90% confidence level is slightly lower than that of the particle filter in both datasets, but not significantly different at the 50% confidence level. Specifically, according to the solution error tables listed in the Appendix B, the difference in RMS error between the filtered solutions from these two filters remains within 1 metre in approximately 50% of the segments in the datasets. The largest differences are found in the C10_E and C2_E data segments for the City of London, and in Epochs 200 to 600 for Canary Wharf.

The difference between 3DMA GNSS grid filtering and particle filtering is more significant in terms of computational load. The computational load of the 3DMA GNSS filters depends mainly on the number of candidates to be computed in each epoch. The count of candidate positions can therefore be used to roughly evaluate the efficiency of these filters. For the 3DMA particle filter, the number of candidate positions is the number of particles maintained. Whereas for the 3DMA grid filter, the number of candidate points may vary, depending on the size and spacing of the grid and the proportion of buildings in the region. The shape and size of the grid can be specified in advance or based on the uncertainty of the position solution from the previous epoch. For example, a circular grid with a radius of 20 metres and a spacing of 1 metre has approximately 1256 candidate points. If the area occupied by buildings is removed, then the actual number of candidates to be computed is even less. Therefore, the average of the counts is suitable for comparison. The number of particles in the particle filter is determined by the minimum number (in steps of 500) that completely covers all the candidate positions in a search area spaced at 1 m and of the same radius.

Returning to the results for the Canary Wharf dataset used in this paper, the particle filter processed 5000 candidate positions per epoch, while the grid filter processed an average of 3604 candidate positions per epoch. For the City of London dataset, the particle filter computed 1000 candidates per epoch, while the grid filter computed an average of only 523 candidates per epoch. Therefore, extrapolating from the number of candidate positions in each epoch, 3DMA GNSS grid filtering should be approximately 40% to 50% faster than 3DMA GNSS particle filtering. However, this is not always true in a practical implementation. In the static positioning test, i.e. the City of London dataset, the grid filtering was indeed almost twice as efficient as the particle filtering. However, in the vehicle navigation test at Canary Wharf, grid filtering consumed as much time as particle filtering, as it traversed all candidate locations (i.e. Equation (38)) when performing the motion-based likelihood redistribution in the system propagation step, which took a significant amount of time and resources.

The problem of getting lost can happen with any filter, and the 3DMA GNSS filters are no exception. The error in the position solution given by a lost filter increases with time, while the uncertainty in the solution remains consistently smaller than the position error. For the 3DMA GNSS filters, the true position lying outside the search area can be defined as getting lost. The lost problem usually starts with an incorrect state estimate. In the specific case of the 3DMA GNSS filters shown in this paper, getting lost can originate from a position and/or velocity solution with large errors. The true position may be too far away from the position prediction given in the system propagation step to lie within the 3DMA GNSS search area in the current epoch. Due

to the limitations of the 3DMA GNSS core algorithm itself, the true position must lie within the search area. Otherwise, it is impossible for the 3DMA GNSS algorithm to provide the correct position solution. Once the true position wanders outside the search area, it is difficult for the lost filter to get the correct position and velocity solution again, and thus difficult to recover in subsequent epochs. Therefore, improving the positioning accuracy of the 3DMA GNSS core algorithm can reduce the chances of the filter getting lost. However, any algorithm can fail in some situations. Artificially expanding the search area to include the true position retains the opportunity for a lost filter to recover in subsequent epochs. Other methods of detecting and recovering lost 3DMA GNSS filters are worth investigating in future research.

V. CONCLUSIONS

The results show that filtering has a greater impact on the results of mobile positioning with significant movement compared to static positioning. In vehicle tests, the conventional GNSS filtering algorithms improve positioning accuracy by more than 40% compared to conventional single-epoch GNSS, while in static positioning they offer only a slight improvement. The advantages of 3DMA GNSS are more apparent in denser environments than in more open areas. In the single epoch positioning of the Canary Wharf dataset, 3DMA GNSS improves the overall RMS position error by about a quarter. But in more open areas, such as the City of London and the non-central areas of Canary Wharf, it doesn't bring much benefit.

3DMA GNSS techniques and filtering algorithms benefit from each other. The former provides the latter with a better position solution in the measurement update step, while the latter in turn rewards the former with a better initial position and a smaller search area. In the Canary Wharf dataset, the filtered 3DMA GNSS solution shows a further reduction in position error of approximately 53% compared to the single-epoch 3DMA GNSS. The filtered results with the 3DMA GNSS techniques reduce the overall RMS error and the maximum error at 90% confidence level by approximately 40% and 60%, respectively, compared to the conventional filtering solution. It can be inferred that multi-epoch 3DMA GNSS filtering should maximise the benefits for mobile positioning in dense environments.

3DMA GNSS grid filtering and particle filtering show similar performance in position accuracy. In terms of efficiency, 3DMA GNSS grid filtering is able to achieve solutions with fewer particles with errors comparable to those of 3DMA GNSS particle filtering. Theoretically grid filtering should consume less resources and run faster than particle filtering. However, the grid filtering in the practical implementation may be slowed down by traversing all candidate positions in the system propagation.

VI. FUTURE WORK

There is much room for improvement in the 3DMA GNSS filtering algorithm, which can be explored in terms of both accuracy and efficiency. Areas that could be investigated include

- Improvements to the 3DMA GNSS algorithms, e.g. optimising the satellite visibility prediction, and improving the scoring models for LBR and SM.
- Detection and recovery of the getting lost problem.
- Adding outlier detection to the 3DMA GNSS core algorithm and the filtering algorithm.
- Improving the efficiency of the system propagation step in GNSS grid filtering.

ACKNOWLEDGEMENTS

Qiming Zhong is funded by the China Scholarship Council and a UCL Engineering Faculty Scholarship. The authors also thank Focal Point Positioning for the conventional pseudo-ranges generated by their software receiver and Imperial College London for use of their trials van and reference system.

APPENDIX A DETAILED DESCRIPTION OF ALGORITHMS

This appendix provides more details of the 3DMA positioning algorithms used to generate the results presented in the paper. As the equipment used differs in the two datasets mentioned in this paper, a set of tuning parameters is applied to each dataset individually.

A.1 3DMA Core Algorithms

The input to the core 3DMA algorithm is a 3D city model of a region and a series of candidate positions within the region, and the output is a scoring surface (also known as likelihood distribution) over these candidates. The score for each candidate position is obtained by the following four algorithms.

a Visibility Prediction

Once a grid of candidate positions has been set up, the visibility of the satellites at these candidates can be predicted. The same set of predictions is used in all subsequent algorithms including shadow matching and likelihood-based ranging. For each candidate position, the probability that the satellite is predicted to be direct line-of-sight (LOS), $p(LOS|BB)$, is determined using the building boundaries precomputed from the 3D mapping data. For the City of London dataset, $p(LOS|BB)$ is set to 0.85 where the satellite elevation is above the building boundary and 0.15 otherwise. For the Canary Wharf dataset, $p(LOS|BB)$ is set to 0.8 and 0.2 for satellites predicted to be LOS and NLOS, respectively. These values account for the possibility that predictions may be wrong due to errors and resolution limitations in the 3D city model and unpredictable factors such as passing vehicles.

b Shadow Matching

Once a set of candidate positions and the satellite visibility predictions at them have been determined, shadow matching comprises the following steps:

1. The probability, $p(LOS|C/N_0)$, that each received signal is direct LOS is determined from the GNSS receiver's C/N_0 measurements using the following statistical model:

$$p(LOS|C/N_0) = \begin{cases} p_{o-\min} & (C/N_0) \leq s_{\min} \\ a_0 + a_1(C/N_0) + a_2[(C/N_0)]^2 & s_{\min} < (C/N_0) < s_{\max} \\ p_{o-\max} & (C/N_0) \geq s_{\max} \end{cases} \quad (6)$$

   where the coefficients are given in Tables 1 and 2.

2. Each candidate position and satellite is then scored according to the match between the predicted and measured satellite visibility.

$$p_m = 1 - p(LOS|C/N_0) - p(LOS|BB) + 2p(LOS|C/N_0)p(LOS|BB) \quad (7)$$

3. An overall likelihood score, Λ_{Sp}, for each position, p, is obtained by multiplying the scores for each satellite.

Table 1: Tuning parameters for determining LOS probability from measured C/N_0 in City of London

Elevation, θ	Satellites	$s_{\min}$, dB-Hz	$s_{\max}$, dB-Hz	$p_{o-\min}$	a_0	a_1, dB-Hz^{-1}	a_2, dB-Hz^{-2}	$p_{o-\max}$
$0° \leq \theta \leq 90°$	All	27	44	0.15	0.4549	-0.0444	0.0012	0.85

Table 2: Tuning parameters for determining LOS probability from measured C/N_0 in Canary Wharf

Elevation, θ	Satellites	$s_{\min}$, dB-Hz	$s_{\max}$, dB-Hz	$p_{o-\min}$	a_0	a_1, dB-Hz^{-1}	a_2, dB-Hz^{-2}	$p_{o-\max}$
$\theta \leq 20°$	All	16	32	0.2	-0.4170	0.0374	0	0.8
$20° \leq \theta \leq 60°$	GPS	26	40	0.2	-0.8369	0.0406	0	0.8
$20° \leq \theta \leq 60°$	Galileo	21	34	0.2	0.6333	-0.0632	0.0020	0.8
$\theta \geq 60°$	All	33	40	0.2	-2.7850	0.0897	0	0.8

c Likelihood-based Ranging

Once a set of candidate positions and the satellite visibility predictions at them have been determined, the likelihood-based ranging algorithm comprises the following steps:

1. For each candidate position, the satellites are ranked based on the elevation angle, measured C/N_0 and surrounding buildings, and the one with the highest score is selected as the reference. The score is calculated by

$$r_j = \frac{1}{n_p}\sum_{p=1}^{n_p}\left(\theta_j - BB_p\right) \times \text{round}\left(\left(C/N_0\right)_j/5\right) \times 5 \tag{8}$$

where j denotes the j^{th} satellite, $\frac{1}{n_p}\sum_{p=1}^{n_p}\left(\theta_j - BB_p\right)$ is the average value of the difference between the satellite elevation, θ_j, and the corresponding building boundary, BB_p, at the candidate point, $p = 1$, and its immediate neighbours, $p = 2, 3, \cdots, n_p$. The neighbours whose distance to the candidate point is less than 1.5 times the grid spacing are considered.

2. At each candidate position, measurement innovations are obtained by subtracting the computed direct LOS ranges (refer to [8] for calculations) from the measured pseudo-ranges and then differencing with respect to the reference satellite to eliminate the receiver clock offset. Note that some known errors, such as atmospheric delays and satellite clock offsets, have been modelled in the calculation of the range to each satellite at the candidate positions.

3. The error standard deviation of all errors except for the NLOS path delay is computed as a function of C/N_0 using,

$$\sigma_j = \sqrt{a \times 10^{-\left(C/N_0\right)_j/10} + b} \tag{9}$$

where a and b are empirically determined constants.

4. At each candidate position, the measurement innovations for satellites predicted to be LOS are modelled by a normal distribution with a mean of μ_L, while those for satellites predicted to be NLOS are modelled by a skew-normal distribution with the location, ξ_N, scale, ω_N and shape, α_N, as follows,

$$\xi_N = \mu_L + \mu_N - \sqrt{\frac{2\sigma_N^2\left(\sigma_j^2 + \sigma_r^2 + \sigma_N^2\right)}{\pi\left(\sigma_j^2 + \sigma_r^2\right) + (\pi - 2)\sigma_N^2}} \tag{10}$$

$$\omega_N = \sqrt{\frac{\left(\sigma_j^2 + \sigma_r^2 + \sigma_N^2\right)^2}{\sigma_j^2 + \sigma_r^2 + (1 - 2/\pi)\,\sigma_N^2}} \tag{11}$$

$$\alpha_N = \sqrt{\frac{\sigma_N^2}{\sigma_j^2 + \sigma_r^2}} \tag{12}$$

where μ_N and σ_N are the mean and standard deviation of the NLOS path delay, respectively, and σ_r is the error standard deviation of the reference satellite, given in Table 3. The cumulative probability, F, of the NLOS measurement innovation, δz_{pj}, is then computed using

$$F = \frac{1}{2}\left[1 + \text{erf}\left(\frac{\delta z_{pj} - \xi_N}{\omega_N\sqrt{2}}\right)\right] - 2T\left(\frac{\delta z_{pj} - \xi_N}{\omega_N}, \alpha_N\right) \tag{13}$$

where $\text{erf}(x)$ is the integral of the normal distribution and $T(x, \alpha)$ is Owen's T function.

The modified measurement innovation, $\delta z'_{pj}$, is then obtained by solving

$$F = \frac{1}{2}\left[1 + \text{erf}\left(\frac{\delta z'_{pj}}{\sqrt{2\left(\sigma_j^2 + \sigma_r^2\right)}}\right)\right] \tag{14}$$

For measurements predicted to be direct LOS, the measurement innovation remains unchanged, i.e., $\delta z'_{pj} = \delta z_{pj}$.

5. To prevent excessively large innovations producing very low likelihood scores, limiting is applied to each innovation

$$\delta z'_{pj} = \max\left(-\delta z_{\max}, \min\left(\delta z_{\max}, \delta z'_{pj} - \mu_L\right)\right) \tag{15}$$

where $\delta z_{\max}$ is given in the Table 3.

6. A likelihood score for each candidate position, p, is finally computed using

$$\Lambda_{Rp} = \exp\left(-\delta \mathbf{z}'^{\mathrm{T}}_p \mathbf{C}^{-1}_{\delta \mathbf{z},p} \delta \mathbf{z}'_p\right) \tag{16}$$

where $\delta \mathbf{z}'_p$ is the vector of re-mapped measurement innovations and $\mathbf{C}_{\delta \mathbf{z},p}$ is the measurement error covariance matrix, given by,

$$\mathbf{C}_{\delta \mathbf{z},p} = \begin{bmatrix} \sigma_1^2 + \sigma_r^2 & \sigma_r^2 & \cdots & \sigma_r^2 \\ \sigma_r^2 & \sigma_2^2 + \sigma_r^2 & \cdots & \sigma_r^2 \\ \vdots & \vdots & \ddots & \vdots \\ \sigma_r^2 & \sigma_r^2 & \cdots & \sigma_m^2 + \sigma_r^2 \end{bmatrix} \tag{17}$$

Table 3: Parameters used in the likelihood-based ranging (LBR) algorithm

Dataset	a, m^2	b, m^2	μ_N, m	σ_N, m	μ_L, m	σ_r, m	$\delta z_{\max}$, m
City of London	9.03×10^4	40.73	18.50	19.00	0	3.00	29.00
Canary Wharf	1.41×10^4	28.10	26.06	31.76	-5.25	2.36	22.00

d Hypothesis Domain Integration

Hypothesis domain integration combines the shadow matching and likelihood-based ranging scores to give a single score for each candidate position:

$$\tilde{\Lambda}_p = \Lambda_{Rp} \Lambda_{Sp}^{W_p} \tag{18}$$

where W_p is the weighting factor, which is a value related to the number of LOS signals in the current epoch.

$$W_p = \frac{\alpha \times n_{LOS,p}}{n_{LOS,p} + n_{NLOS,p}} \tag{19}$$

where $n_{LOS,p}$ and $n_{NLOS,p}$ are the number of satellites predicted to be LOS and NLOS at candidate position p, respectively, and α is an empirically determined constant. For the City of London dataset, α takes a value of 4.6, while for the Canary Wharf dataset, α is 3.6.

A.2 3DMA Filtering Algorithms

This appendix shows several important components of the 3DMA filtering algorithm excluding the 3DMA core algorithm (described separately in Appendix A.1). Some of these components, i.e., initialisation and velocity filtering, are required for both particle filtering and grid filtering, while others are only used in grid filtering as the equivalent components are available in conventional particle filtering. For example, 3DMA particle filtering can use the conventional system propagation scheme directly. Note that the velocity initialisation and velocity filtering can be omitted in static positioning.

a Initialisation

The initialisation is divided into position and velocity components, where the position is initialised by a standard single-epoch 3DMA GNSS algorithm set and the velocity is initialised by a weighted least squares method with 3DMA outlier detection. For static positioning applications, the velocity is considered known and does not need to be initialised.

The single-epoch 3DMA GNSS for position initialisation consists of three steps: the weighted least squares ranging is used to determine a rough position solution, from which a grid of candidate positions are generated, and finally the core 3DMA GNSS algorithm scores these candidates to derive a position solution. The detailed algorithm is described in [14], and the 3DMA GNSS core algorithm and parameters can also be found in the Appendix A.1.

The velocity initialisation comprises the following steps:

1. For each candidate position, predict the satellite visibility using the building boundaries. Note that the predictions are already made in the 3DMA GNSS positioning algorithm and can therefore be used directly here without recalculation.
2. The overall LOS probability of a satellite over the search area is calculated by

$$p_{LOS}^{j} = \frac{\sum_p \tilde{\Lambda}_{p,0} \delta_{LOS,p,0}^{j}}{\sum_p \tilde{\Lambda}_{p,0}} \tag{20}$$

   where j denotes the satellite, $\tilde{\Lambda}_{p,0}$ is the likelihood of candidate position p, and $\delta_{LOS,p,0}^{j}$ is a Boolean value representing the predicted visibility of satellite j at candidate position p.

3. Pseudo-range rate measurements are then selected from satellites that meet the criteria $p_{LOS}^{j} \geq T_{LOS}$, where the threshold T_{LOS} is determined empirically and is given in Table 4.
4. The standard deviation (STD) of the measurement error for each of the conforming satellites is determined using

$$\sigma_{r,j} = \sigma_{r0} \left[1 + \beta \left(1 - p_{LOS}^{j} \right) \right] \tag{21}$$

   where the coefficients σ_{r0} and β are determined empirically and are given in Table 4.
5. The measurement innovation, $\delta \mathbf{z}_0^-$, is

$$\delta \mathbf{z}_0^- = \begin{bmatrix} \tilde{\dot{\rho}}_a^1 - \hat{\dot{r}}_{a1}^- \\ \tilde{\dot{\rho}}_a^2 - \hat{\dot{r}}_{a2}^- \\ \vdots \\ \tilde{\dot{\rho}}_a^j - \hat{\dot{r}}_{aj}^- \end{bmatrix} \tag{22}$$

   where $\tilde{\dot{\rho}}_a^j$ is the measured pseudo-range rate from satellite j, and $\hat{\dot{r}}_{aj}^-$ is the predicted range rate for satellite j after eliminating known errors such as the effect of Earth rotation, calculated using the method in [8].

   The measurement matrix, $\mathbf{H}_{G,0}^{e}$, is computed using

$$\mathbf{H}_{G,0}^{e} = \begin{bmatrix} -\hat{u}_{a1,x}^{e} & -\hat{u}_{a1,y}^{e} & -\hat{u}_{a1,z}^{e} & 1 \\ -\hat{u}_{a2,x}^{e} & -\hat{u}_{a2,y}^{e} & -\hat{u}_{a2,z}^{e} & 1 \\ \vdots & \vdots & \vdots & \vdots \\ -\hat{u}_{aj,x}^{e} & -\hat{u}_{aj,y}^{e} & -\hat{u}_{aj,z}^{e} & 1 \end{bmatrix} \tag{23}$$

   where $\hat{\mathbf{u}}_{aj}^{e} = \begin{bmatrix} \hat{u}_{aj,x}^{e} & \hat{u}_{aj,y}^{e} & \hat{u}_{aj,z}^{e} \end{bmatrix}$ is the line-of-sight unit vector of satellite j, calculated using the method in [8].

   The measurement error covariance matrix, $\mathbf{C}_r$, is given by

$$\mathbf{C}_r = \begin{bmatrix} \sigma_{r,1}^2 & 0 & \cdots & 0 \\ 0 & \sigma_{r,2}^2 & \cdots & 0 \\ \vdots & \vdots & \ddots & \vdots \\ 0 & 0 & \cdots & \sigma_{r,j}^2 \end{bmatrix} \tag{24}$$

   The velocity state vector consists of the velocity, $\hat{\mathbf{v}}_{ea,0}^{e+}$, and the clock drift, $\delta \hat{\dot{\rho}}_{c,0}^{a+}$, and is obtained by

$$\hat{\mathbf{x}}_0^+ = \begin{bmatrix} \hat{\mathbf{v}}_{ea,0}^{e+} \\ \delta \hat{\dot{\rho}}_{c,0}^{a+} \end{bmatrix} = \left({\mathbf{H}_{G,0}^{e}}^{\mathrm{T}} \mathbf{C}_r^{-1} \mathbf{H}_{G,0}^{e} \right)^{-1} {\mathbf{H}_{G,0}^{e}}^{\mathrm{T}} \mathbf{C}_r^{-1} \delta \mathbf{z}_0^- \tag{25}$$

and the state estimation error covariance is initialised using

$$\mathbf{P}_0^+ = \left({\mathbf{H}_{G,0}^e}^{\mathrm{T}} \mathbf{C}_r^{-1} \mathbf{H}_{G,0}^e \right)^{-1} \tag{26}$$

6. The east and north velocities are then given by

$$\mathbf{v}_{EN,0}^+ = \begin{bmatrix} \hat{v}_{ea,E,0}^{n+} \\ \hat{v}_{ea,N,0}^{n+} \end{bmatrix} = \begin{bmatrix} 0 & 1 & 0 \\ 1 & 0 & 0 \end{bmatrix} \mathbf{C}_e^n \hat{\mathbf{v}}_{ea,0}^{e+} \tag{27}$$

and their error covariance is

$$\mathbf{P}_{vE,vN,0}^+ = \begin{bmatrix} 0 & 1 & 0 \\ 1 & 0 & 0 \end{bmatrix} \mathbf{C}_e^n \mathbf{P}_{0,1:3,1:3}^+ \mathbf{C}_n^e \begin{bmatrix} 0 & 1 \\ 1 & 0 \\ 0 & 0 \end{bmatrix} \tag{28}$$

where $\mathbf{P}_{0,1:3,1:3}^+$ is the first three columns and rows of $\mathbf{P}_0^+$.

The north-east-down (NED) to Earth-centered Earth-fixed (ECEF) coordinate transformation matrix, $\mathbf{C}_e^n$, in Equations (27) and (28) is given by

$$\mathbf{C}_e^n = \begin{bmatrix} -\sin L_a \cos \lambda_a & -\sin L_a \sin \lambda_a & \cos L_a \\ -\sin \lambda_a & \cos \lambda_a & 0 \\ -\cos L_a \cos \lambda_a & -\cos L_a \sin \lambda_a & -\sin L_a \end{bmatrix} \tag{29}$$

where the latitude, L_a, and longitude, λ_a, are obtained from the position solution, while $\mathbf{C}_n^e = {\mathbf{C}_e^n}^{\mathrm{T}}$ is the ECEF to NED coordinate transformation matrix.

Table 4: Parameters used in the initialisation of 3DMA filtering

T_{LOS}	σ_{r0}	β
0.2	0.2	5

Note that since the users in the City of London dataset are stationary, these velocity parameters are not required.

b System Propagation

System propagation predicts the state estimate of the next epoch based on currently known information, which moves position candidates and redistributes their likelihoods. The process is divided into the following three steps:

1. The search area is expanded to ensure that candidates with high scores from the previous epoch (or initialisation) fall in the centre of the search area in subsequent calculations. In the case of a circular search area, for example, the radius r_p is increased to $r_q = 2r_p$ with the same centre.

   Thus, likelihoods for the candidate positions within the expanded area, indexed by q, are initialised using

$$\Lambda_{q,k}^0 = \begin{cases} \Lambda_{p,k-1=q,k}^+ & q_k \in P_{k-1} \\ 0 & q_k \notin P_{k-1} \end{cases} \tag{30}$$

   where $\Lambda_{p,k-1=q,k}^+$ is the likelihood at the preceding epoch, $k-1$, following the position measurement update, of the point p_{k-1} that has the same coordinates as point qk, and P_{k-1} is the set of candidate positions used for the position measurement update at epoch $k-1$.

   The coordinate notation of the candidate position is also updated after the search area extension to avoid confusion.

$$\begin{aligned} E_{q,k}^0 &= E_{p,k} \\ N_{q,k}^0 &= N_{p,k} \end{aligned} \tag{31}$$

2. The position estimate between epochs can be propagated by a velocity solution and its associated error covariance. The predicted displacement between epochs $k-1$ and k is

$$\begin{bmatrix} \Delta\hat{E}_k^- \\ \Delta\hat{N}_k^- \end{bmatrix} = \begin{bmatrix} \hat{v}_{eb,E,k-1}^{n+} \\ \hat{v}_{eb,N,k-1}^{n+} \end{bmatrix} \tau_s \tag{32}$$

where $\hat{v}_{eb,E,k-1}^{n+}$ and $\hat{v}_{eb,N,k-1}^{n+}$ are, respectively, the estimated east and north velocities at epoch $k-1$, and τ_s is the time interval between epochs.

The error covariance of the predicted displacement is

$$\mathbf{P}_{\Delta E,\Delta N,k}^- = \begin{bmatrix} \sigma_{\Delta E}^2 & P_{\Delta E\Delta N} \\ P_{\Delta E\Delta N} & \sigma_{\Delta N}^2 \end{bmatrix} = \mathbf{P}_{vE,vN,k-1}^+ \tau_s^2 + \frac{1}{3}\begin{bmatrix} S_{aE,k} & S_{aEN,k} \\ S_{aEN,k} & S_{aN,k} \end{bmatrix} \tau_s^3 \tag{33}$$

where $\mathbf{P}_{vE,vN,k-1}^+$ is the error covariance of the east and north velocities at the preceding epoch $k-1$, $S_{aE,k}$ and $S_{aN,k}$ are the power spectral densities (PSDs) of the east and north accelerations respectively, and $S_{aEN,k}$ is the cross spectral density of the east and north accelerations. The same values as in the velocity filter, given by (55), are used.

To facilitate alignment with the grid in the search area, the displacement is partitioned into integer grid space $\hat{e}_k^-, \hat{n}_k^-$ and remainder $\delta\hat{E}_k^-, \delta\hat{N}_k^-$ components:

$$\begin{aligned} \Delta\hat{E}_k^- &= \hat{e}_k^- \Delta p_g + \delta\hat{E}_k^- \\ \Delta\hat{N}_k^- &= \hat{n}_k^- \Delta p_g + \delta\hat{N}_k^- \end{aligned} \tag{34}$$

where Δp_g is the grid spacing, and the integer part is given by

$$\begin{aligned} \hat{e}_k^- &= \text{round}\left(\Delta\hat{E}_k^- / \Delta p_g\right) \\ \hat{n}_k^- &= \text{round}\left(\Delta\hat{N}_k^- / \Delta p_g\right) \end{aligned} \tag{35}$$

The position likelihood is redistributed to account for the integer displacement simply by changing the position associated with each likelihood. Thus,

$$\begin{aligned} E_{q,k}^1 &= E_{q,k}^0 + \hat{e}_k^- \Delta p_g \\ N_{q,k}^1 &= N_{q,k}^0 + \hat{n}_k^- \Delta p_g \end{aligned} \tag{36}$$

$$\Lambda_{q,k}^1\left(E_{q,k}^1, N_{q,k}^1\right) = \Lambda_k^0\left(E_{q,k}^0, N_{q,k}^0\right) \tag{37}$$

For the remainder part, the likelihoods are then redistributed using

$$\Lambda_{q,k}^2 = \sum_{i=-m_E}^{m_E} \sum_{j=-m_N}^{m_N} w_{ijk} \Lambda_k^1\left(E_{q,k}^1 + i\Delta p_g, N_{q,k}^1 + j\Delta p_g\right) \tag{38}$$

where the weighting for each epoch is computed by

$$w_{ijk} = \frac{w'_{ijk}}{\sum_{i=-m_E}^{m_E} \sum_{j=-m_N}^{m_N} w'_{ijk}} \tag{39}$$

where

$$w'_{ijk} = \exp\left(-\frac{1}{2}\begin{bmatrix} i\Delta p_g - \delta\hat{E}_k^- \\ j\Delta p_g - \delta\hat{N}_k^- \end{bmatrix}^{\mathrm{T}} \left(\mathbf{P}_{\Delta E,\Delta N,k}^-\right)^{-1} \begin{bmatrix} i\Delta p_g - \delta\hat{E}_k^- \\ j\Delta p_g - \delta\hat{N}_k^- \end{bmatrix}\right) \tag{40}$$

and

$$\begin{aligned} m_E &= \text{ceiling}\left(3\sigma_{\Delta E}/\Delta p_g\right) \\ m_N &= \text{ceiling}\left(3\sigma_{\Delta N}/\Delta p_g\right) \end{aligned} \tag{41}$$

In static positioning, since the velocity of the receiver is known to be zero, the motion-based likelihood redistribution does not need to be performed. Thus, the coordinates and likelihoods of the candidate positions are inherited directly from the expanded search area:

$$\begin{aligned} E^1_{q,k} &= E^0_{q,k} \\ N^1_{q,k} &= N^0_{q,k} \end{aligned} \tag{42}$$

$$\Lambda^2_{q,k} = \Lambda^1_{q,k} = \Lambda^0_{q,k} \tag{43}$$

3. The confidence-based likelihood redistribution adds a minimum likelihood to all candidates in the search area. Let C_P be the level of confidence in the position solution from the preceding epoch (or initialisation), where $0 < C_P < 1$. The likelihoods are redistributed using

$$\Lambda^-_{q,k} = \Lambda^2_{q,k} + \frac{\Delta p_g^2}{A_p} \frac{1 - C_P}{C_P} \tag{44}$$

where A_p is the area of the search area calculated by

$$A_p = \pi r_p^2 \tag{45}$$

for a circular area with radius, r_p, or by

$$A_p = \pi a_p b_p \tag{46}$$

for an elliptical area with semi-major axis, a_p, and semi-minor axis, b_p. C_P takes a value of 0.99 in both the City of London and Canary Wharf datasets.

c Search Area Determination

The centre of the search area for the 3DMA GNSS position measurement corresponds to the weighted average position solution obtained from the propagated likelihood grid, giving by

$$\begin{aligned} \hat{E}^-_k &= \frac{\sum_q \Lambda^-_{q,k} E^1_{q,k}}{\sum_q \Lambda^-_{q,k}} \\ \hat{N}^-_k &= \frac{\sum_q \Lambda^-_{q,k} N^1_{q,k}}{\sum_q \Lambda^-_{q,k}} \end{aligned} \tag{47}$$

The likelihood of the candidate positions remains unchanged within the newly defined search area. Thus, the notation is updated by

$$\Lambda^-_{p,k} = \Lambda^-_{q,k=p,k} \tag{48}$$

The size of the search area can be fixed, or vary with the error covariance. In the City of London and Canary Wharf tests, the search area was fixed to a circular area of 20m and 40m radius, respectively.

d Position Measurement Update

At each candidate position, the likelihood is updated with the propagated likelihood, $\Lambda^-_{p,k}$, and the 3DMA scoring, $\tilde{\Lambda}_{p,k}$, by

$$\Lambda'_{p,k} = \Lambda^-_{p,k} \left(\tilde{\Lambda}_{p,k} \right)^{W_m} \tag{49}$$

where W_m is the empirically determined measurement weighting factor. A value greater than 1 gives more weighting to new measurement data while a value less than 1 gives less. W_m takes a value of 1 for both the City of London and Canary Wharf datasets. The overall likelihood is then normalised by

$$\Lambda^+_{p,k} = \frac{\Lambda'_{p,k}}{\sum_p \Lambda'_{p,k}} \tag{50}$$

Finally, the updated position solution is obtained using

$$\begin{aligned}\hat{E}_k^+ &= \sum_p \Lambda_{p,k}^+ E_{p,k} \\ \hat{N}_k^+ &= \sum_p \Lambda_{p,k}^+ N_{p,k}\end{aligned} \tag{51}$$

where $E_{p,k}$ and $N_{p,k}$ are the easting and northing coordinates of the p^{th} candidate position.

e Velocity Filter

The velocity filter includes prediction and update steps. In the propagation step, with no additional information, the velocity state estimates remain unchanged, while the error covariance increases. Thus,

$$\hat{\mathbf{x}}_k^- = \begin{bmatrix} \hat{\mathbf{v}}_{ea,k}^{e-} \\ \delta\hat{\rho}_{c,k}^{a-} \end{bmatrix} = \hat{\mathbf{x}}_{k-1}^+ = \begin{bmatrix} \hat{\mathbf{v}}_{ea,k-1}^{e+} \\ \delta\hat{\rho}_{c,k-1}^{a+} \end{bmatrix} \tag{52}$$

$$\mathbf{P}_k^- = \mathbf{P}_{k-1}^+ + \begin{bmatrix} \mathbf{S}_{a,k}^e \tau_s & \mathbf{0}_{3\times 1} \\ \mathbf{0}_{1\times 3} & S_{cf}^a \tau_s \end{bmatrix} \tag{53}$$

where S_{cf}^a is the receiver clock frequency drift PSD, τ_s is the time interval between epochs, and $\mathbf{S}_{a,k}^e$ is the acceleration PSD matrix that is given by

$$\mathbf{S}_{a,k}^e = \mathbf{C}_n^e \begin{bmatrix} S_{aN,k} & S_{aEN,k} & 0 \\ S_{aEN,k} & S_{aE,k} & 0 \\ 0 & 0 & S_{aD,k} \end{bmatrix} \mathbf{C}_e^n \tag{54}$$

where $\mathbf{C}_e^n$ and $\mathbf{C}_n^e$ are transformation matrices between NED and ECEF coordinates as shown in Equation (29), $S_{aE,k}$ is the east acceleration PSD, $S_{aN,k}$ is the north acceleration PSD, $S_{aEN,k}$ is the cross spectral density of the east and north accelerations, and $S_{aD,k}$ is the vertical acceleration PSD.

For a typical vehicle, the acceleration is similar in the Easting and Northing directions, while the vertical acceleration is relatively small. The horizontal acceleration tends to be greater at lower speeds. Therefore, the acceleration PSD model is proposed as follows

$$\begin{aligned} S_{aE,k} = S_{aN,k} &= \begin{cases} \dfrac{\left(55 - \left|\hat{\mathbf{v}}_{ea,k}^{e-}\right|\right)^2}{100} K_a & \left|\hat{\mathbf{v}}_{ea,k}^{e-}\right| \leq 50 \text{ m/s} \\ 0.25 K_a & \left|\hat{\mathbf{v}}_{ea,k}^{e-}\right| > 50 \text{ m/s} \end{cases} \\ S_{aEN,k} &= 0 \\ S_{aD,k} &= 0.25 K_a \end{aligned} \tag{55}$$

where the constant, $K_a = 1.5 m^2/s^3$, is determined empirically.

In the measurement update step, the weighting model applied to the measurement errors is similar to the one used in the velocity initialisation shown in Equations (20) and (21), which is given by

$$p_{LOS}^j = \frac{\sum_p \tilde{\Lambda}_{p,k} \delta_{LOS,p,k}^j}{\sum_p \tilde{\Lambda}_{p,k}} \tag{56}$$

$$\sigma_{r,j} = \sigma_{r0} \left[1 + \beta \left(1 - p_{LOS}^j\right)\right] \tag{57}$$

Note that measurements with a predicted LOS probability, p_{LOS}, lower than the threshold, T_{LOS}, are discarded.

The measurement noise covariance, $\mathbf{R}_k$, is then obtained using

$$\mathbf{R}_k = \begin{bmatrix} \sigma_{r,1}^2 & 0 & \cdots & 0 \\ 0 & \sigma_{r,2}^2 & \cdots & 0 \\ \vdots & \vdots & \ddots & \vdots \\ 0 & 0 & \cdots & \sigma_{r,j}^2 \end{bmatrix} \tag{58}$$

The measurement matrix, $\mathbf{H}_{G,k}^e$, is given by

$$\mathbf{H}_{G,k}^e = \begin{bmatrix} -\hat{u}_{a1,k,x}^e & -\hat{u}_{a1,k,y}^e & -\hat{u}_{a1,k,z}^e & 1 \\ -\hat{u}_{a2,k,x}^e & -\hat{u}_{a2,k,y}^e & -\hat{u}_{a2,k,z}^e & 1 \\ \vdots & \vdots & \vdots & \vdots \\ -\hat{u}_{aj,k,x}^e & -\hat{u}_{aj,k,y}^e & -\hat{u}_{aj,k,z}^e & 1 \end{bmatrix} \tag{59}$$

where $\hat{\mathbf{u}}_{aj,k}^e$ is the line-of-sight unit vector of satellite j.

The Kalman gain is then computed using

$$\mathbf{K}_k = \mathbf{P}_k^- {\mathbf{H}_{G,k}^e}^{\mathrm{T}} \left(\mathbf{H}_{G,k}^e \mathbf{P}_k^- {\mathbf{H}_{G,k}^e}^{\mathrm{T}} + \mathbf{R}_k \right)^{-1} \tag{60}$$

The measurement innovation, $\delta \mathbf{z}_k^-$, is computed using

$$\delta \mathbf{z}_k^- = \begin{bmatrix} \tilde{\rho}_{a,k}^1 - \hat{\dot{r}}_{a1,k}^- - \delta \hat{\dot{\rho}}_{c,k}^{a-} \\ \tilde{\rho}_{a,k}^2 - \hat{\dot{r}}_{a2,k}^- - \delta \hat{\dot{\rho}}_{c,k}^{a-} \\ \vdots \\ \tilde{\rho}_{a,k}^j - \hat{\dot{r}}_{aj,k}^- - \delta \hat{\dot{\rho}}_{c,k}^{a-} \end{bmatrix} \tag{61}$$

where $\tilde{\dot{\rho}}_{a,k}^j$ is the measured pseudo-range rate from satellite j, $\hat{\dot{r}}_{aj,k}^-$ is the modelled range rate from satellite j, and $\delta \hat{\dot{\rho}}_{c,k}^{a-}$ is the predicted receiver clock drift.

The state estimate consisting of the velocity, $\hat{\mathbf{v}}_{ea,k}^{e+}$, and clock drift, $\delta \hat{\dot{\rho}}_{c,k}^{a+}$, is then updated using

$$\hat{\mathbf{x}}_k^+ = \begin{bmatrix} \hat{\mathbf{v}}_{ea,k}^{e+} \\ \delta \hat{\dot{\rho}}_{c,k}^{a+} \end{bmatrix} = \hat{\mathbf{x}}_k^- + \mathbf{K}_k \delta \mathbf{z}_k^- \tag{62}$$

The state estimation error covariance is updated using

$$\mathbf{P}_k^+ = \left(\mathbf{I} - \mathbf{K}_k \mathbf{H}_{G,k}^e \right) \mathbf{P}_k^- \tag{63}$$

The east and north velocity and their error covariance can then be obtained using Equations (27-29).

APPENDIX B DETAILED EXPERIMENTAL RESULTS

Tables 5 and 6 show in detail the horizontal radial position root mean square (RMS) errors for various positioning algorithms in the City of London and Canary Wharf, respectively. The numbers in brackets in the first column of Table 6 represent the counts of epochs where vehicles were located in the central area of Canary Wharf.

Table 5: Horizontal radial position RMS errors (in metres) for different algorithms in City of London

Experiment ID	Single-epoch conventional	Single-epoch 3DMA	Conventional GNSS EKF	Conventional GNSS PF	3DMA GNSS PF	3DMA GNSS GF
C1_W	8.13	7.60	4.42	7.30	6.37	7.82
C1_E	5.37	2.70	3.62	5.26	2.05	1.72
C2_W	13.47	14.38	7.21	10.71	10.50	7.86
C2_E	10.07	11.91	9.76	9.64	10.05	6.98
C3	13.69	2.74	2.97	7.37	4.54	4.15
C4	5.36	2.43	5.33	5.54	2.41	1.76
C5	6.13	4.28	5.04	5.91	4.33	3.09
C6	2.91	3.41	2.19	2.46	2.43	1.52
C7	6.10	4.74	3.37	5.30	1.77	2.05
C8	16.25	21.67	14.40	18.39	14.56	7.97
C9_W	14.07	4.87	12.14	14.53	5.86	8.45
C9_E	12.86	8.53	9.25	8.58	4.14	3.23
C10_W	11.23	5.79	12.63	10.37	3.87	2.64
C10_E	17.56	12.88	14.02	16.66	15.98	9.53
C11	12.89	1.82	6.93	9.96	2.78	3.46
C12_N	9.15	5.16	7.14	9.28	6.89	6.12
C12_S	9.32	3.92	5.76	10.01	3.83	4.35
C13_N	12.37	28.15	8.24	10.13	38.84	42.83
C13_S	23.88	10.14	27.32	22.85	15.03	16.15
C14_W	15.75	5.51	7.90	20.01	7.70	10.37
C14_E	13.33	6.72	6.26	12.40	6.68	6.69
C15_W	13.75	18.80	12.58	12.50	12.66	14.63
C15_E	32.68	21.31	28.77	23.91	11.99	11.12

Table 6: Horizontal radial position RMS errors (in metres) for different algorithms in Canary Wharf

Epoch range	Single-epoch conventional	Single-epoch 3DMA	Conventional GNSS EKF	Conventional GNSS PF	3DMA GNSS PF	3DMA GNSS GF
1-200 (0)	21.52	19.89	5.87	8.38	9.03	8.53
201-400 (0)	40.01	36.36	45.60	56.74	21.56	12.39
401-600 (139)	66.83	26.58	29.80	16.91	32.06	37.40
601-800 (27)	14.86	18.34	26.93	19.22	15.41	16.50
801-1000 (144)	66.27	49.62	13.51	17.50	9.21	8.76
1001-1200 (124)	84.52	68.28	39.95	33.60	12.39	9.52
1201-1400 (27)	12.48	15.14	24.20	18.08	13.57	13.86
1401-1602 (0)	4.79	5.71	5.77	7.68	5.36	4.89

Tables 7, 8, 9, and 10 list the maximum horizontal radial errors for the position solutions of the different algorithms at different confidence intervals respectively. The numbers in brackets in the first column of Tables 8 and 10 represent the counts of epochs where vehicles were located in the central area of Canary Wharf.

Table 7: Maximum horizontal radial position error (in metres) for different algorithms in City of London, 90% of confidence

Experiment ID	Single-epoch conventional	Single-epoch 3DMA	Conventional GNSS EKF	Conventional GNSS PF	3DMA GNSS PF	3DMA GNSS GF
C1_W	13.29	14.08	5.66	11.82	10.61	9.88
C1_E	8.91	3.88	4.81	7.76	3.00	2.31
C2_W	19.95	16.48	9.22	15.82	16.96	12.21
C2_E	14.06	14.82	12.04	12.76	14.54	7.75
C3	21.73	4.12	4.13	11.31	6.42	5.63
C4	8.93	3.03	6.29	9.00	3.29	2.49
C5	8.41	6.60	6.47	7.53	6.00	4.78
C6	4.07	4.15	3.64	3.94	3.02	1.71
C7	10.10	6.16	5.22	8.52	2.63	3.11
C8	25.47	33.49	18.03	27.83	19.61	11.16
C9_W	18.99	5.78	13.75	19.48	4.78	17.49
C9_E	19.56	10.19	10.80	12.34	5.86	5.65
C10_W	15.99	7.22	14.70	15.37	5.47	3.56
C10_E	24.04	25.71	14.47	23.50	40.26	16.11
C11	19.16	3.27	10.33	15.49	4.55	4.24
C12_N	12.58	6.91	9.25	12.84	7.89	7.70
C12_S	13.64	5.32	8.25	14.65	5.57	6.51
C13_N	21.05	32.40	10.77	17.52	47.96	47.95
C13_S	31.84	21.26	28.47	28.13	32.00	31.42
C14_W	25.26	7.23	8.87	32.12	10.09	12.84
C14_E	19.81	8.81	7.75	17.67	8.14	9.04
C15_W	19.29	32.48	15.70	16.67	24.59	30.58
C15_E	44.10	28.87	38.97	40.96	17.23	15.51

Table 8: Maximum horizontal radial position error (in metres) for different algorithms in Canary Wharf, 90% of confidence

Epoch range	Single-epoch conventional	Single-epoch 3DMA	Conventional GNSS EKF	Conventional GNSS PF	3DMA GNSS PF	3DMA GNSS GF
1-200 (0)	22.26	22.85	9.47	13.99	13.92	13.82
201-400 (0)	76.77	51.58	82.27	104.03	18.83	15.72
401-600 (139)	147.54	55.27	53.46	27.60	63.52	81.68
601-800 (27)	20.71	24.01	58.46	17.13	18.67	23.61
801-1000 (144)	74.82	29.49	24.23	31.44	13.56	12.70
1001-1200 (124)	151.18	79.45	82.97	64.04	16.94	15.45
1201-1400 (27)	21.17	12.46	55.76	22.57	12.12	11.01
1401-1602 (0)	5.90	8.51	10.23	12.82	8.15	7.35

Table 9: Maximum horizontal radial position error (in metres) for different algorithms in City of London, 50% of confidence

Experiment ID	Single-epoch conventional	Single-epoch 3DMA	Conventional GNSS EKF	Conventional GNSS PF	3DMA GNSS PF	3DMA GNSS GF
C1_W	6.35	5.78	4.20	5.83	5.32	7.18
C1_E	3.86	2.42	4.05	4.75	1.76	1.56
C2_W	12.88	15.25	7.19	9.44	7.99	5.92
C2_E	9.52	11.87	8.50	9.86	9.84	6.90
C3	10.38	2.32	3.01	6.02	4.28	3.57
C4	4.68	2.33	5.69	4.45	2.28	1.15
C5	5.75	3.99	4.82	5.97	4.05	2.54
C6	2.63	3.51	1.64	2.11	2.40	1.50
C7	4.12	3.16	3.03	3.42	1.34	2.07
C8	13.64	18.18	14.59	15.34	13.53	8.53
C9_W	13.28	1.53	13.16	13.98	2.25	5.62
C9_E	10.90	8.62	8.95	8.77	4.04	2.40
C10_W	10.64	5.62	12.51	9.52	3.72	3.00
C10_E	16.76	6.03	14.15	15.31	7.77	5.82
C11	9.73	0.84	5.54	7.81	1.67	3.73
C12_N	8.53	5.16	7.26	8.29	6.46	6.87
C12_S	9.13	4.32	4.89	9.50	3.15	4.92
C13_N	8.44	30.74	8.98	7.65	34.58	47.38
C13_S	23.52	2.93	27.70	22.92	3.92	3.35
C14_W	11.57	5.30	7.84	16.09	7.48	9.69
C14_E	10.48	6.32	5.84	8.68	6.46	5.87
C15_W	10.82	12.94	10.97	9.44	7.87	10.47
C15_E	34.92	21.33	29.88	16.05	10.56	10.58

Table 10: Maximum horizontal radial position error (in metres) for different algorithms in Canary Wharf, 50% of confidence

Epoch range	Single-epoch conventional	Single-epoch 3DMA	Conventional GNSS EKF	Conventional GNSS PF	3DMA GNSS PF	3DMA GNSS GF
1-200 (0)	5.26	4.14	4.76	5.68	4.02	4.00
201-400 (0)	5.86	6.17	26.63	29.17	6.12	6.13
401-600 (139)	12.45	9.85	6.99	10.99	9.92	9.17
601-800 (27)	3.85	3.38	10.80	5.12	3.33	3.60
801-1000 (144)	9.93	5.78	6.89	9.81	5.59	5.54
1001-1200 (124)	15.34	7.58	7.04	8.26	7.03	7.30
1201-1400 (27)	3.01	4.28	9.70	9.03	4.38	5.31
1401-1602 (0)	2.55	3.71	4.86	5.57	3.68	3.62

REFERENCES

[1] M. Usman, M. R. Asghar, I. S. Ansari, F. Granelli, and K. A. Qaraqe, "Technologies and Solutions for Location-Based Services in Smart Cities: Past, Present, and Future," *IEEE Access*, vol. 6, pp. 22 240–22 248, apr 2018.

[2] European GSA, "GNSS User Technology Report Issue 2," *European Global Navigation Satellite Systems Agency*, no. 2, p. 92, 2018. [Online]. Available: https://www.gsa.europa.eu/system/files/reports/gnss_user_tech_report_2018.pdf

[3] F. van Diggelen, "Google's Use of 3D Building Models to Solve Urban GNSS," 2021. [Online]. Available: https://www.ion.org/itm/abstracts.cfm?paperID=10048

[4] P. D. Groves, "Shadow matching: A new GNSS positioning technique for urban canyons," *Journal of Navigation*, vol. 64, no. 3, pp. 417–430, jul 2011.

[5] K. Nur, S. Feng, C. Ling, and W. Ochieng, "Integration of GPS with a WiFi high accuracy ranging functionality," *Geo-Spatial Information Science*, vol. 16, no. 3, pp. 155–168, sep 2013. [Online]. Available: http://www.tandfonline.com/doi/abs/10.1080/10095020.2013.817106

[6] P. Groves, L. Wang, M. Adjrad, and C. Ellul, "GNSS shadow matching: The challenges ahead," in *Proceedings of the 28th International Technical Meeting of The Satellite Division of the Institute of Navigation (ION GNSS+ 2015). (pp. 2421-2443).* The Institute of Navigation, sep 2015.

[7] S. Ji, W. Chen, X. Ding, Y. Chen, C. Zhao, and C. Hu, "Potential benefits of GPS/GLONASS/GALILEO integration in an urban canyon - Hong Kong," *Journal of Navigation*, vol. 63, no. 4, pp. 681–693, oct 2010.

[8] P. D. Groves, *Principles of GNSS, inertial, and multisensor integrated navigation systems*. Boston; London: Artech House, 2013.

[9] P. D. Groves, Z. Jiang, M. Rudi, and P. Strode, "A portfolio approach to NLOS and multipath mitigation in dense urban areas," *26th International Technical Meeting of the Satellite Division of the Institute of Navigation, ION GNSS 2013*, vol. 4, no. September, pp. 3231–3247, 2013.

[10] N. I. Ziedan, "Urban positioning accuracy enhancement utilizing 3D buildings model and accelerated ray tracing algorithm," *30th International Technical Meeting of the Satellite Division of the Institute of Navigation, ION GNSS 2017*, vol. 5, pp. 3253–3268, 2017.

[11] H. F. Ng, G. Zhang, and L. T. Hsu, "A Computation Effective Range-Based 3D Mapping Aided GNSS with NLOS Correction Method," *Journal of Navigation*, vol. 73, no. 6, pp. 1202–1222, nov 2020. [Online]. Available: https://doi.org/10.1017/S037346332000003X

[12] E. D. Kaplan and C. Hegarty, *Understanding GPS/GNSS: Principles and Applications*, 3rd ed. Artech House Inc, 2017.

[13] P. Misra and P. Enge, *Global positioning system : signals, measurements, and performance*. Ganga-Jamuna Press, 2010.

[14] P. D. Groves, Q. Zhong, R. Faragher, and P. Esteves, "Combining Inertially-aided Extended Coherent Integration (Supercorrelation) with 3D-Mapping- Aided GNSS," in *Proceedings of ION GNSS+ 2020. Institute of Navigation (ION): Virtual conference. (2020) (In press).* Institute of Navigation (ION), sep 2020. [Online]. Available: https://www.ion.org/gnss/

[15] L. T. Hsu, Y. Gu, and S. Kamijo, "3D building model-based pedestrian positioning method using GPS/GLONASS/QZSS and its reliability calculation," *GPS Solutions*, vol. 20, no. 3, pp. 413–428, 2016.

[16] T. Suzuki and N. Kubo, "Correcting GNSS multipath errors using a 3D surface model and particle filter," *26th International Technical Meeting of the Satellite Division of the Institute of Navigation, ION GNSS 2013*, vol. 2, pp. 1583–1595, 2013.

[17] L. Wang, P. D. Groves, and M. K. Ziebart, "Smartphone shadow matching for better cross-street GNSS positioning in urban environments," *Journal of Navigation*, vol. 68, no. 3, pp. 411–433, 2015.

[18] T. Suzuki, "Integration of GNSS positioning and 3D map using particle filter," *29th International Technical Meeting of the Satellite Division of the Institute of Navigation, ION GNSS 2016*, vol. 2, pp. 1296–1304, 2016.

[19] N. I. Ziedan, "Enhancing GNSS mobile positioning in urban environments through utilization of multipath prediction and consistency analysis," *Proceedings of the 32nd International Technical Meeting of the Satellite Division of the Institute of Navigation, ION GNSS+ 2019*, pp. 3469–3483, 2019.

[20] A. Kornhauser, "Global Navigation Satellite System (GNSS)," Princeton University, Tech. Rep., 2006. [Online]. Available: https://www.princeton.edu/$\sim$alaink/Orf467F07/GNSS.pdf

[21] P. D. Groves, Z. Jiang, L. Wang, and M. K. Ziebart, "Intelligent Urban Positioning using Multi-Constellation GNSS with 3D Mapping and NLOS Signal Detection," *Ieee Transactions On Aerospace*, pp. 458–472, 2012.

[22] L. Wang, "Investigation of Shadow Matching for GNSS Positioning in Urban Canyons," Ph.D. dissertation, University College London, 2015.

[23] T. Kos, I. Markezic, and J. Pokrajcic, "Effects of multipath reception on GPS positioning performance," in *Proceedings Elmar - International Symposium Electronics in Marine*, 2010, pp. 399–402. [Online]. Available: https://ieeexplore.ieee.org/document/5606130

[24] P. D. Groves and Z. Jiang, "Height aiding, C/N0 weighting and consistency checking for gnss nlos and multipath mitigation in urban areas," *Journal of Navigation*, vol. 66, no. 5, pp. 653–669, sep 2013.

[25] J. H. Amt and J. F. Raquet, "Positioning for range-based land navigation systems using surface topography," in *Proceedings of the Institute of Navigation - 19th International Technical Meeting of the Satellite Division, ION GNSS 2006*, vol. 3, sep 2006, pp. 1494–1505. [Online]. Available: http://www.ion.org/publications/abstract.cfm?jp=p&articleID=6773

[26] J. Bradbury, M. Ziebart, P. A. Cross, P. Boulton, and A. Read, "Code multipath modelling in the urban environment using large virtual reality city models: Determining the local environment," *Journal of Navigation*, vol. 60, no. 1, pp. 95–105, jan 2007. [Online]. Available: https://www.cambridge.org/core/product/identifier/S0373463307004079/type/journal_article

[27] T. Suzuki and N. Kubo, "Simulation of GNSS Satellite Availability in Urban Environments Using Google Earth," *Proceedings of the ION 2015 Pacific PNT Meeting*, pp. 1069 – 1079, 2015.

[28] L. Wang, P. D. Groves, and M. K. Ziebart, "Multi-constellation GNSS performance evaluation for urban canyons using large virtual reality city models," *Journal of Navigation*, vol. 65, no. 3, pp. 459–476, jul 2012.

[29] L. T. Hsu, Y. Gu, and S. Kamijo, "NLOS correction/exclusion for GNSS measurement using RAIM and city building models," *Sensors (Switzerland)*, vol. 15, no. 7, pp. 17 329–17 349, jul 2015. [Online]. Available: http://www.mdpi.com/1424-8220/15/7/17329

[30] R. Ercek, P. De Doncker, and F. Grenez, "NLOS-multipath effects on pseudo-range estimation in Urban canyons for GNSS applications," in *European Space Agency, (Special Publication) ESA SP*, vol. 626 SP. European Space Agency, 2006.

[31] Y. Gu and S. Kamijo, "GNSS positioning in deep urban city with 3D map and double reflection," in *2017 European Navigation Conference, ENC 2017*. Institute of Electrical and Electronics Engineers Inc., jun 2017, pp. 84–90.

[32] G. Zhang, H.-F. Ng, W. Wen, and L.-T. Hsu, "3D Mapping Database Aided GNSS Based Collaborative Positioning Using Factor Graph Optimization," *IEEE Transactions on Intelligent Transportation Systems*, pp. 1–13, apr 2020.

[33] D. Betaille, F. Peyret, M. Ortiz, S. Miquel, and L. Fontenay, "A new modeling based on urban trenches to improve GNSS positioning quality of service in cities," *IEEE Intelligent Transportation Systems Magazine*, vol. 5, no. 3, pp. 59–70, 2013.

[34] C. Tiberius and E. Verbree, "GNSS positioning accuracy and availability within Location Based Services: The advantages of combined GPS-Galileo positioning," in *NaviTec*, 2004.

[35] S. S. Saab and Z. M. Kassas, "Power matching approach for GPS coverage extension," *IEEE Transactions on Intelligent Transportation Systems*, vol. 7, no. 2, pp. 156–166, 2006.

[36] B. Ben-Moshe, E. Elkin, H. Levi, and A. Weissman, "Improving accuracy of GNSS devices in urban canyons," *Proceedings of the 23rd Annual Canadian Conference on Computational Geometry, CCCG 2011*, 2011.

[37] L. Wang, P. D. Groves, and M. K. Ziebart, "GNSS Shadow Matching Using A 3D Model of London," in *European Navigation Conference*, dec 2011.

[38] L. Wang, P. D. Groves, and M. Ziebart, "Urban positioning on a smartphone: Real-time shadow matching using GNSS and 3D City Models," *26th International Technical Meeting of the Satellite Division of the Institute of Navigation, ION GNSS 2013*, vol. 2, pp. 1606–1619, sep 2013.

[39] P. D. Groves, L. Wang, and M. Ziebart, "Shadow matching: Improved GNSS accuracy in Urban canyons," *GPS World*, vol. 23, no. 2, 2012.

[40] J. T. Isaacs, A. T. Irish, F. Quitin, U. Madhow, and J. P. Hespanha, "Bayesian localization and mapping using GNSS SNR measurements," in *Record - IEEE PLANS, Position Location and Navigation Symposium*, 2014, pp. 445–451.

[41] G. Zhang, W. Wen, B. Xu, and L. T. Hsu, "Extending Shadow Matching to Tightly-Coupled GNSS/INS Integration System," *IEEE Transactions on Vehicular Technology*, vol. 69, no. 5, pp. 4979–4991, may 2020.

[42] L. Wang, "Kinematic GNSS Shadow Matching Using a Particle Filter," *Ion Gnss+*, 2014.

[43] R. Yozevitch and B. ben Moshe, "A Robust Shadow Matching Algorithm for GNSS Positioning," *Navigation, Journal of the Institute of Navigation*, vol. 62, no. 2, pp. 95–109, sep 2015. [Online]. Available: http://doi.wiley.com/10.1002/navi.85

[44] M. Obst, S. Bauer, and G. Wanielik, "Urban multipath detection and mitigation with dynamic 3D maps for reliable land vehicle localization," in *Record - IEEE PLANS, Position Location and Navigation Symposium*, 2012, pp. 685–691.

[45] S. Peyraud, D. Bètaille, S. Renault, M. Ortiz, F. Mougel, D. Meizel, and F. Peyret, "About non-line-of-sight satellite detection and exclusion in a 3D map-aided localization algorithm," *Sensors (Switzerland)*, vol. 13, no. 1, pp. 829–847, 2013.

[46] H. F. Ng and L. T. Hsu, "3D Mapping Database Aided GNSS RTK and Its Assessments in Urban Canyons," *IEEE Transactions on Aerospace and Electronic Systems*, 2021.

[47] N. Kbayer, M. Sahmoudi, H. Ortega, and Ć. Rouch, "Approximate maximum likelihood estimation using a 3d gnss simulator for positioning in mp/nlos conditions," in *30th International Technical Meeting of the Satellite Division of the Institute of Navigation, ION GNSS 2017*, vol. 5, 2017, pp. 3039–3052.

[48] P. D. Groves, "Draft Algorithm Specification for Multi-Epoch 3DMA GNSS Ranging," University College London, 2018.